Materials Today • Volume xxx, Number xx • xxxx 2021 RESEARCH

ELSEVIER

RESEARCH: Review

Crystal defect modulation in cathode materials for non-lithium ion batteries: Progress and challenges

Fangyu Xiong [1], Shuangshuang Tan [1], Xuhui Yao [3], Qinyou An [1,2,*], Liqiang Mai [1,2,*]

[1] State Key Laboratory of Advanced Technology for Materials Synthesis and Processing, Wuhan University of Technology, Wuhan, 430070, China
[2] Foshan Xianhu Laboratory of the Advanced Energy Science and Technology Guangdong Laboratory, Foshan 528200, Guangdong, China
[3] Advanced Technology Institute, University of Surrey, Guildford, Surrey GU2 7XH, United Kingdom

Non-lithium ion (Na/K/Mg/Ca/Zn/Al-ion) batteries (NLIBs) have stepped into the spotlight as alternatives or supplements to lithium-ion batteries in large-scale energy storage systems with the aid of vast advantages in resource and production cost. In the past years, a lot of efforts have been taken to develop high-performance cathode materials for various NLIBs by exploiting new cathode materials or optimizing the existing categories. As an efficient optimizing strategy to break the bottleneck of intrinsic lattice, crystal defect modulation attracts much attention and has been applied in many cathode materials. Suitable crystal defects in cathode materials could enhance the electrochemical reactivity, electronic conductivity, ionic diffusivity, and structural stability, then improving the capacity, rate performance and cycling stability of batteries. In this review, the investigations of crystal defect modulation in cathode materials for NLIBs are systematically summarized by highlighting some typical and recent progresses. The positive effects and improvement mechanism of intentionally introduced defects, including substitutional impurity, interstitial impurity, vacancy defect, cation disorder and amorphization, are discussed. Besides, the challenges and the perspectives about future directions of crystal defect modulation on the cathode materials for NLIBs are presented.

Introduction

Given the growing concern on the exhaustion of fossil fuels and environmental issues, the exploitation and commercialization of renewable energy become one of the most attractive solutions, supplying the increasing demand of energy consumption in the meantime. However, owing to the intermittence and regional inequality of potential renewable energy resources, such as solar, tide and wind energy, the large-scale energy storage systems (LSESSs) are essential for rational utilization of renewable energy [1,2]. Lithium-ion batteries (LIBs) have dominated the market of power source of mobile electronic equipment and electric vehicle by virtues of high energy density and remarkable energy efficiency, while their application in LSEESs has met the frustration due to the high cost and limited Li resource [3–9]. Therefore, non-lithium ion (such as Na/K/Mg/Ca/Zn/Al-ion) batteries (NLIBs) with abundant resource and potential low cost have attracted increasing attention in the recent years [10–16]. Those NLIBs have been considered as promising alternatives or supplements to LIBs for the application in LSESSs.

Determined by the fundamental theory and reaction mechanism of metal-ion batteries, cathode material is one of the most important components which have a decisive effect on the electrochemical performance of those batteries [17,18]. Although a series of promising cathode materials have been exploited, the intrinsic electrochemical performances of pristine cathode materials are still far from the demands of practical application. Thus, various strategies, such as nanostructure design, surface coating, and crystal structure regulation, have been employed to improve the electrochemical performance of cathode materials for NLIBs [4,10,19–22]. Crystal defect modulation is a widely used strategy and the intentionally introduced defects play important roles in

* Corresponding authors.
E-mail addresses: An, Q. (anqinyou86@whut.edu.cn), Mai, L. (mlq518@whut.edu.cn).

1369-7021/© 2020 Elsevier Ltd. All rights reserved. https://doi.org/10.1016/j.mattod.2020.12.002

Please cite this article in press as: F. Xiong et al., Materials Today, (2021), https://doi.org/10.1016/j.mattod.2020.12.002

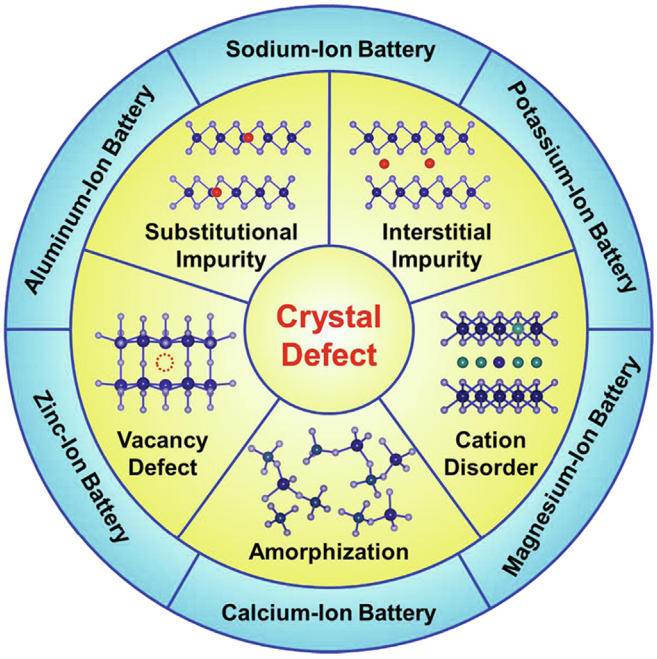

FIGURE 1

Schematic of crystal defect modulation in cathode materials for various NLIBs.

the performance modification, such as enhancing electronic conductivity, reducing ion diffusion energy barrier, suppressing harmful phase transition, improving structural stability and so forth [23–26]. A rich variety of crystal defects endow crystal defect modulation with ability to modify various properties of cathode materials. For example, crystal defect modulation can activate the electrochemical activity of materials by creating ion channels, which is difficult to be achieved by nanostructure design or surface coating strategy. Moreover, compared to nanostructure construction, crystal defect modulation can avoid reducing the tap density, which is beneficial for volumetric energy density. Besides, crystal defect modulation is atomic-scale technology, which can be combined with nanostructure design or surface coating strategy to realize the further improvement on electrochemical performance.

Due to the differences in ionic radius or charge number of non-lithium ions compared to Li ions, there are many differences in the cathode materials of LIBs and NLIBs. In the same systems, the diffusion barriers for lithium-ion and non-lithium ions will be different. Therefore, for NLIBs, especially multivalent-ion batteries, larger ion diffusion channels were desired. Moreover, some cathode materials of NLIBs may display totally different properties with their Li counterpart. For example, the phase transition of layered oxide cathode materials for SIBs during the charging/discharging process is more complex compared to the Li counterpart, $LiFePO_4$ is one of the most successful cathode materials for LIBs while thermodynamically stable $NaFePO_4$ was considered as electrochemically inactive in SIBs, as well as $LiCrO_2$ is electrochemically inactive while $NaCrO_2$ is active [18,27,28]. Besides, the categories of promising cathode materials for multivalent-ion batteries are different with that of LIBs. Layered lithium metal oxides and some phosphates (such as $LiFePO_4$) are the most promising cathode materials, while their counterparts in multivalent-ion batteries are barely satisfactory. Due to these differences, the cathode materials for NLIBs have different challenges and problems with that for LIBs. Therefore, a review focus on crystal defect in cathode materials for NLIBs is necessary, although some reviews have discussed the crystal defects in cathode materials for LIBs. The intentionally introduced crystal defects in the cathode materials for those NLIBs batteries can be mainly classified to substitutional impurity, interstitial impurity, vacancy defect, cation disorder and lattice disorder (amorphization) (Fig. 1). This review strives to clarify the positive effects and work mechanisms of different defects on electrochemical performances, summarize the typical and recent progresses of crystal defect modulation on cathode materials for NLIBs and offer the future directions for developing effective crystal defect modulation.

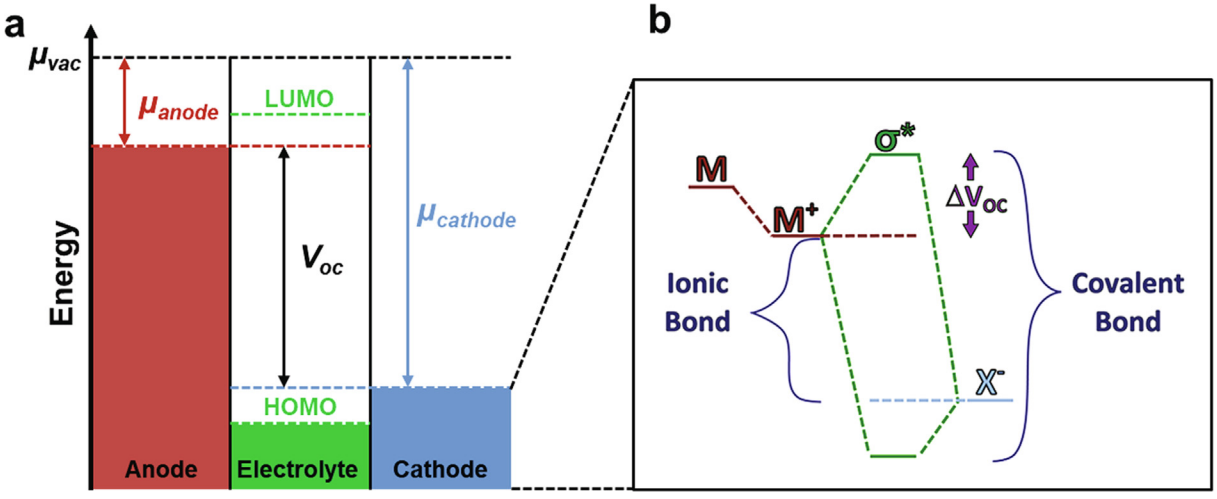

FIGURE 2

Schematic illustration for (a) the energy levels involved in metal-ion battery, and (b) the separation between the bonding (σ) and antibonding (σ*) orbitals in two extreme types of bonds. Reproduced with permission from Ref. [33]. Copyright 2013, American Chemical Society.

Please cite this article in press as: F. Xiong et al., Materials Today, (2021), https://doi.org/10.1016/j.mattod.2020.12.002

TABLE 1

Summary of electrochemical performance of some cathode materials with substitutional impurity for NLIBs.

Substitutional Impurity	Materials	Battery system	Highest specific capacity/ current density (mAh g^{-1}/mA g^{-1})	Average discharge potential (V)	Rate performance (mAh g^{-1}/ mA g^{-1})	Cycling performance (mAh g^{-1}/ *n*/mA g^{-1})	Ref.
Li	$Na_{2.5}Li_{0.5}V_2(PO_4)_3$/C	SIBs	~130/59	~3.3 vs. Na^+/Na	~100/2360	–	[38]
Mg	$Na_{0.67}Mn_{0.67}Ni_{0.28}Mg_{0.05}O_2$	SIBs	123/17.3	~3.5 vs. Na^+/Na	–	104.5/50/17.3	[39]
Mg	$Na_{0.67}Ni_{0.2}Mg_{0.1}Mn_{0.7}O_2$	SIBs	~128/12	~3.3 vs. Na^+/Na	118/400	106.2/50/400	[40]
Mg	$Na_{2/3}Mn_{0.95}Mg_{0.05}O_2$	SIBs	~175/100	~2.6 vs. Na^+/Na	106/5000	~80/100/5000	[41]
Mg	$Na_3V_{1.95}Mg_{0.05}(PO_4)_3$/C	SIBs	112.5/117.6	~3.2 vs. Na^+/Na	94.2/3528	108.4/50/1176	[42]
Mg	$K_{0.7}Mn_{0.7}Mg_{0.3}O_2$	PIBs	144.5/20	~2.4 vs. K^+/K	58.2/400	93.4/400/100	[43]
Mg	$K_{0.45}Ni_{0.1}Co_{0.1}Mg_{0.05}Mn_{0.75}O_2$	PIBs	80.8/20	~2.4 vs. K^+/K	25/500	60/100/20	[44]
Mg and Cu	$Na_{0.67}Mn_{0.71}Cu_{0.02}Mg_{0.02}Ni_{0.25}O_2$	SIBs	160/10	~2.6 vs. Na^+/Na	72/2000	~135/100/20	[45]
Mg and Cu	$Na_{2/3}Mn_{0.72}Cu_{0.22}Mg_{0.06}O_2$	SIBs	107.6/17.4	~3.1 vs. Na^+/Na	73.8/1740	~93/100/174	[46]
Al	$K_{0.45}Ni_{0.1}Co_{0.1}Al_{0.05}Mn_{0.75}O_2$	PIBs	84.5/20	~2.4 vs. K^+/K	37/500	65/100/20	[44]
Al	$Na_{0.6}Ni_{0.22}Al_{0.11}Mn_{0.66}O_2$	SIBs	250/20	~3.0 vs. Na^+/Na	~140/800	~200/50/20	[47]
Al	$Na_3V_{1.8}Al_{0.2}(PO_4)_3$	SIBs	107/23.6	~3.4 vs. Na^+/Na	96.8/708	102.7/60/23.6	[48]
K	$Na_{2.91}K_{0.09}V_2(PO_4)_3$/C	SIBs	110/23.5	~3.35 vs. Na^+/Na	81.4/588	~85/200/117.6	[49]
Ti	$Na_{2/3}Ni_{1/3}Mn_{1/3}Ti_{1/3}O_2$	SIBs	~90/17.3	~3.5 vs. Na^+/Na	~69.7/3460	~73.5/500/173	[50]
Ti	$Na_3V_{1.9}Ti_{0.1}(PO_4)_2F_3$	SIBs	121/65	~3.6 vs. Na^+/Na	~115/5200	91.5/200/130	[51]
Ti	Gradient Ti doped MnO_2	ZIBs	259/100	~1.35 vs. Zn^{2+}/Zn	50/10000	~180/4000/ 1000	[52]
Ti and Cu	$Na_{0.67}Mn_{0.7}Cu_{0.15}Ti_{0.15}O_2$	SIBs	170/20	~2.5 vs. Na^+/Na	85/2000	~85/300/2000	[53]
Cr	$Na_3V_{0.19}Cr_{0.01}(PO_4)_2F_3$@C	SIBs	~110/64	~3.6 vs. Na^+/Na	~65/1280	–	[54]
Mn	$Na_4Mn_1Fe_2(PO_4)_2(P_2O_7)$	SIBs	~110/6.45	~3.1 vs. Na^+/Na	77.4/2580	~66.4/3000/129	[35]
Mn	$Na_3MnV(PO_4)_3$	SIBs	101/101	~3.4 vs. Na^+/Na	~90/1010	90/1000/101	[55]
Fe	$Na_3FeV(PO_4)_3$	SIBs	105/101	~3.2 vs. Na^+/Na	~90/1010	100/1000/101	
Ni	$Na_3NiV(PO_4)_3$	SIBs	~80/101	~3.5 vs. Na^+/Na	~70/505	67/500/505	
Fe	$K_{0.45}Mn_{0.8}Fe_{0.2}O_2$	PIBs	106.2/20	~2.6 vs. K^+/K	64.9/200	44.7/100/200	[56]
Fe	$Na_{2/3}Fe_{2/9}Ni_{2/9}Mn_{5/9}O_2$	SIBs	141/16	~3.55 vs. Na^+/Na	63/800	102.1/100/80	[57]
Fe	$Ni_{0.75}Fe_{0.25}Se_2$	MIBs	190/10	~0.8 vs. Mg^{2+}/Mg	120/50	148/500/20	[58]
Fe and Cu	$Na_{0.9}Cu_{0.22}Fe_{0.30}Mn_{0.48}O_2$	SIBs	100/10	~3.25 vs. Na^+/Na	59/500	97/100/10	[59]
Co	$Na_{0.7}Mn_{0.7}Ni_{0.2}Co_{0.1}O_2$	SIBs	154/12	~2.3 vs. Na^+/Na	70/2400	94/100/240	[60]
Co	$Na_{0.6}Co_{0.1}Mn_{0.9}MnO_2$	SIBs	183/20	~2.4 vs. Na^+/Na	120/400	108.5/150/20	[61]
Co	Gradient $NaNi_{0.60}Co_{0.05}Mn_{0.35}O_2$	SIBs	157/75	~2.7 vs. Na^+/Na	127.3/1500	125.6/300/75	[62]
Co	MnO_2/N-doped carbon cloth	ZIBs	280/1200	~1.3 vs. Zn^{2+}/Zn	30/10500	280/600/1200	[63]
Co and Ni	$Na_{0.66}Ni_{0.13}Mn_{0.54}Co_{0.13}O_2$	SIBs	121/200	~3.5 vs. Na^+/Na	41/3000	~100/150/200	[64]
Co and Ni	$ZnMn_2O_4$@ N-doped reduced graphene oxide	ZIBs	200.5/10	~1.3 vs. Zn^{2+}/Zn	93.5/1500	95.4/900/1000	[65]
Ni	$K_{0.67}Mn_{0.83}Ni_{0.17}O_2$	PIBs	122/20	~2.4 vs. K^+/K	65/500	~53/200/500	[66]
Ni and Cu	$Na_{0.67}Cu_{0.15}Ni_{0.20}Mn_{0.65}O_2$	SIBs	87/10	~3.4 vs. Na^+/Na	78/1000	60/1000/1000	[67]
Cu	$Na_{7/9}Cu_{2/9}Fe_{1/9}Mn_{2/3}O_2$	SIBs	89/10	~3.6 vs. Na^+/Na	51/200	59.5/150/100	[68]
Cu	$Na_{0.6}Mn_{0.9}Cu_{0.1}O_2$	SIBs	~170/20	~2.6 vs. Na^+/Na	85/1600	96/250/800	[69]
Cu	$Na_{0.67}Ni_{0.18}Cu_{0.15}Mn_{0.67}O_2$	SIBs	~120/10	~3.4 vs. Na^+/Na	62/2000	~93/200/10	[70]
Cu	Mn_2O_3	ZIBs	246/50	~1.35 vs. Zn^{2+}/Zn	62/5000	98.5/600/100	[71]
Zn	$Na_{0.66}Ni_{0.26}Zn_{0.07}Mn_{0.67}O_2$	SIBs	~140/12	~3.5 vs. Na^+/Na	~80/768	–	[72]
Zr	$Na_{0.75}Mn_{0.55}Ni_{0.25}Co_{0.05}Fe_{0.10}Zr_{0.05}O_2$	SIBs	143/12	~2.8 vs. Na^+/Na	53/2400	110/100/24	[73]
Y	$Na_3V_{1.9}Y_{0.1}(PO_4)_2F_3$/C	SIBs	121/64	~3.5 vs. Na^+/Na	~80/6400	~112.2/200/128	[74]
Mo	$Na_{2.9}V_{1.98}Mo_{0.02}(PO_4)_3$	SIBs	~110/59	~3.3 vs. Na^+/Na	~92/1180	~80/500/1180	[75]
Mo	$Na_3V_{1.95}Mn_{0.05}(PO_4)_2F_3$@C	SIBs	122.9/25.6	~3.6 vs. Na^+/Na	60.7/1280	109/500/25.6	[76]
F	$Na_{2/3}Ni_{1/3}Mn_{2/3}O_{1.95}F_{0.05}$	SIBs	106.7/17	~3.4 vs. Na^+/Na	86.4/1700	61/2000/1700	[77]
F	$Na_{0.67}Li_{0.1}Fe_{0.4}Mn_{0.5}O_{1.9}F_{0.1}$	SIBs	182/20	~2.8 vs. Na^+/Na	128.7/400	~87/200/200	[78]
F	$NaNi_{1/3}Fe_{1/3}Mn_{1/3}O_{1.99}F_{0.01}$	SIBs	~122/30	~3.1 vs. Na^+/Na	~62/300	~110/70/150	[79]
F	$Na_{0.65}Mn_{0.75}Ni_{0.25}O_{1.9}F_{0.1}$	SIBs	163.7/17	~2.8 vs. Na^+/Na	~108/170	~95/200/85	[80]
F	$Na_3V_{1.98}(PO_4)_{2.9}F_{0.3}$/C	SIBs	116.9/11.8	~3.35 vs. Na^+/Na	92/472	89.8/100/118	[81]
F	$Na_3V_2(PO_4)_{2.93}F_{0.07}$/C	SIBs	109.9/10	~3.35 vs. Na^+/Na	96.9/200	97.8/1000/200	[36]
F	$Na_{2.85}V_2(PO_{3.95}F_{0.05})_3$/C	SIBs	103/100	~3.35 vs. Na^+/Na	69/1000	96/250/100	[82]
F	$MoO_{2.8}F_{0.2}$	MIBs	~76/–	~1.9 vs. Mg^{2+}/Mg	–	–	[83]
S	S-doped V_2O_5	MIBs	~300/50	~1.4 vs. Mg^{2+}/Mg	–	–	[84]
Se	$Mg_xMo_6S_6Se_2$	MIBs	~110/15	~1.15 vs. Mg^{2+}/Mg	~80/122	~100/100/15	[85]
Se	$CuS_{1-x}Se_x$	MIBs	268.5/20	~0.8 vs. Mg^{2+}/Mg	119.2/500	140.7/90/300	[86]
N	$K_{0.6}CoO_{2-x}N_x$	PIBs	86/50	~2.6 vs. K^+/K	30/500	67/400/50	[87]
N	N-doped MnO_{2-x}	ZIBs	286.3/200	~1.35 vs. Zn^{2+}/Zn	121.5/3000	172.7/1000/ 1000	[88]

Please cite this article in press as: F. Xiong et al., Materials Today, (2021), https://doi.org/10.1016/j.mattod.2020.12.002

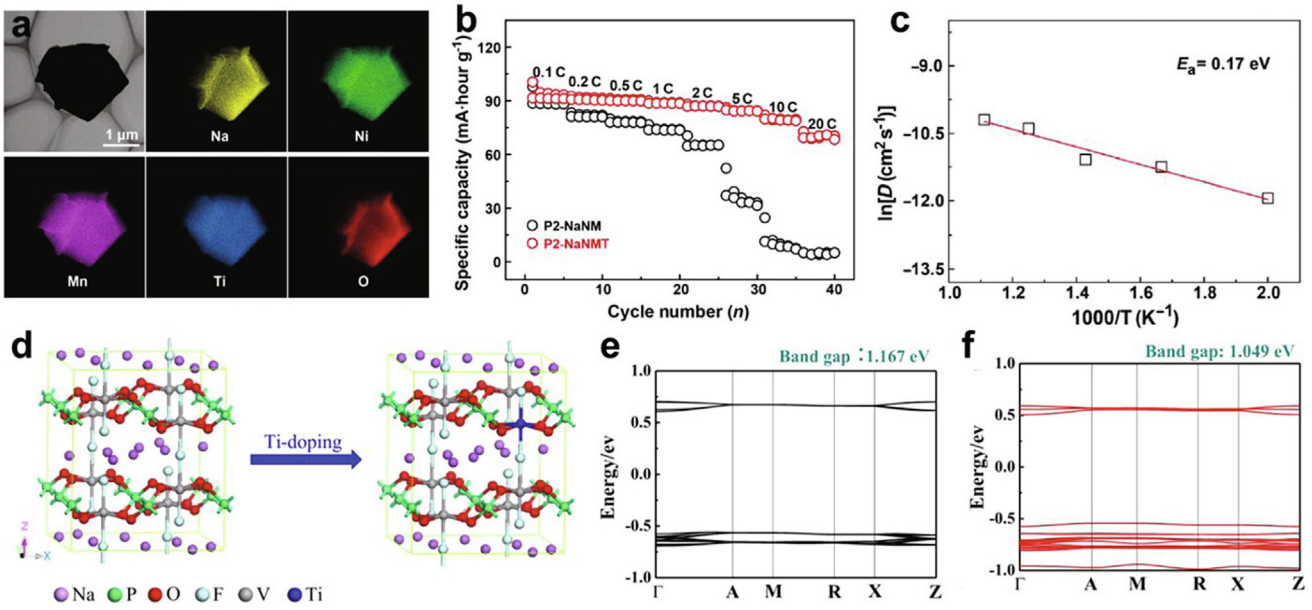

FIGURE 3

(a) Transmission electron microscopy (TEM) image and energy disperse spectroscopy (EDS) elemental mappings of P2-$Na_{2/3}Ni_{1/3}Mn_{1/3}Ti_{1/3}O_2$ (b) The rate performance of Ti-doped P2-$Na_{2/3}Ni_{1/3}Mn_{1/3}Ti_{1/3}O_2$ and undoped P2-$Na_{2/3}Ni_{1/3}Mn_{2/3}O_2$; (c) The Arrhenius plot of Na^+ diffusion coefficients of P2-$Na_{2/3}Ni_{1/3}Mn_{1/3}Ti_{1/3}O_2$. Reproduced with permission from Ref. [50]. Copyright 2018, American Association for the Advancement of Science. (d) Crystal structure model of pristine and Ti-doped $Na_3V_2(PO_4)_2F_3$; The band structure of (e) pristine and (f) Ti-doped $Na_3V_2(PO_4)_2F_3$. Reproduced with permission from Ref. [51]. Copyright 2018, Elsevier Ltd.

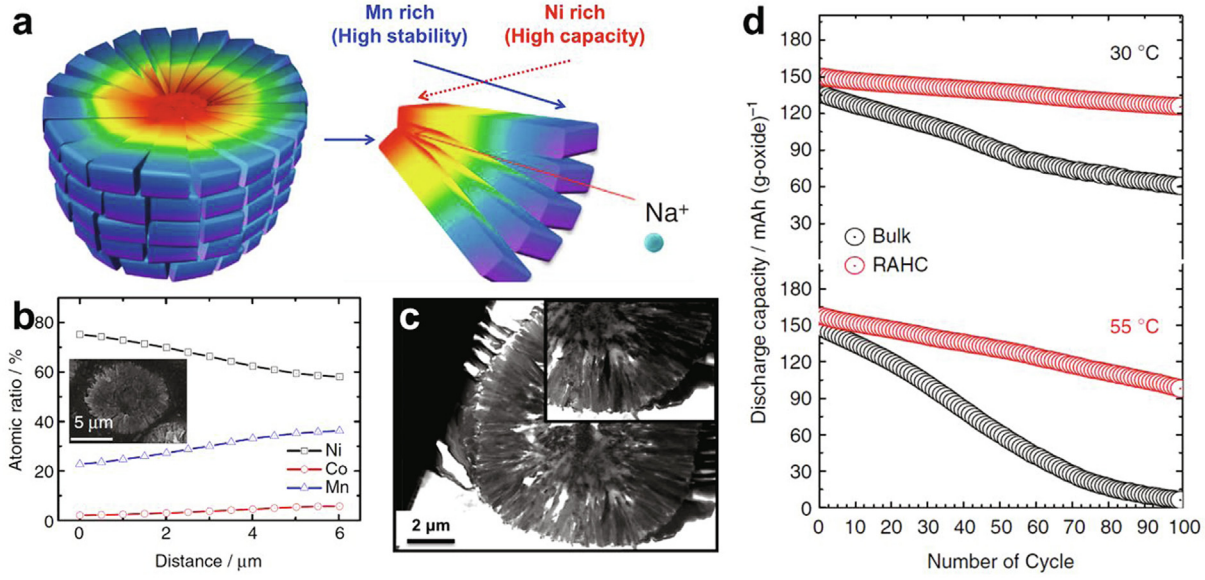

FIGURE 4

(a) The structural illustration, (b) Electron probe microanalysis (EPMA) results (inset: cross-sectional SEM image), and (c) cross-sectional TEM image of gradient substituted $Na[Ni_{0.60}Co_{0.05}Mn_{0.35}]O_2$; (d) The cycling performance of bulk and gradient substituted $Na[Ni_{0.60}Co_{0.05}Mn_{0.35}]O_2$. Reproduced with permission from Ref. [62]. Copyright 2015, Macmillan Publishers Limited.

Roles and fundamental principles of crystal defects in cathode materials

In the second law of thermodynamics perspective, "ideal crystals" do not exist in the nature and the crystal defects are indispensable. Actually, the crystal defects can directly impact both the chemical and physical properties of solid-state materials. For cathode materials of metal-ion batteries, the crystal defects are able to affect the electrochemical behaviors by altering both thermodynamics and kinetics. In this section, the major roles of crystal defects in cathode materials for NLIBs related fundamental principles are summarized.

Please cite this article in press as: F. Xiong et al., Materials Today, (2021), https://doi.org/10.1016/j.mattod.2020.12.002

Accelerating ion diffusion

The ion diffusion is the essential process in the electrochemical reactions of the most cathode materials for NLIBs. The ion diffusion rate is very important for the electrochemical activity and rate performance of cathode materials and usually described by ion diffusion coefficient (D). D depends to the hop distance (λ) between adjacent sites, the hop frequency (ω) and the geometric factor (ρ) that relates to the symmetry of the sublattice of interstitial sites. Their relationship can be described as following [29,30]:

$$D = \rho\lambda^2\omega \quad (1)$$

The ω can be written as: [29–31]

$$\omega = \upsilon^* \exp\left(-\frac{\Delta E}{kT}\right) \quad (2)$$

where υ* is a vibrational factor, ΔE is diffusion energy barrier, k is Boltzmann constant and T is temperature. Both experimental and theoretical studies confirmed that suitable crystal defects such as impurities and vacancies in cathode materials can lower ΔE. According to the Eqs. (1) and (2), D has an exponential correlation on ΔE. Therefore, a small reduction in diffusion energy barrier (ΔE) resulted from crystal defects will translates into a large increase in ion diffusion coefficient (D).

Promoting electron transfer

For high-performance cathode materials, both high ion diffusion coefficient and high electronic conductivity are desired. The electrochemical reaction kinetics is restrained by one of the slower side of the ion diffusion and the electron transfer. Doping, introducing impurity defects, has been demonstrated as an efficient way to modify the electronic conductivity of materials. The presence of impurity atoms will generate the impurity energy level, which may reduce the energy required by electron transition and increase the electronic conductivity. Moreover, introducing interstitial impurities or oxygen vacancies can partially reduce transition metal to achieve mixed-valence states due to the charge compensation effect, tunning the electronic conductivity of materials. [23,24]

Modifying potential

The voltage of metal-ion batteries is related to the potentials of anode and cathode materials (Fig. 2a). During the discharge process, the electrons located at the Fermi level of anode material

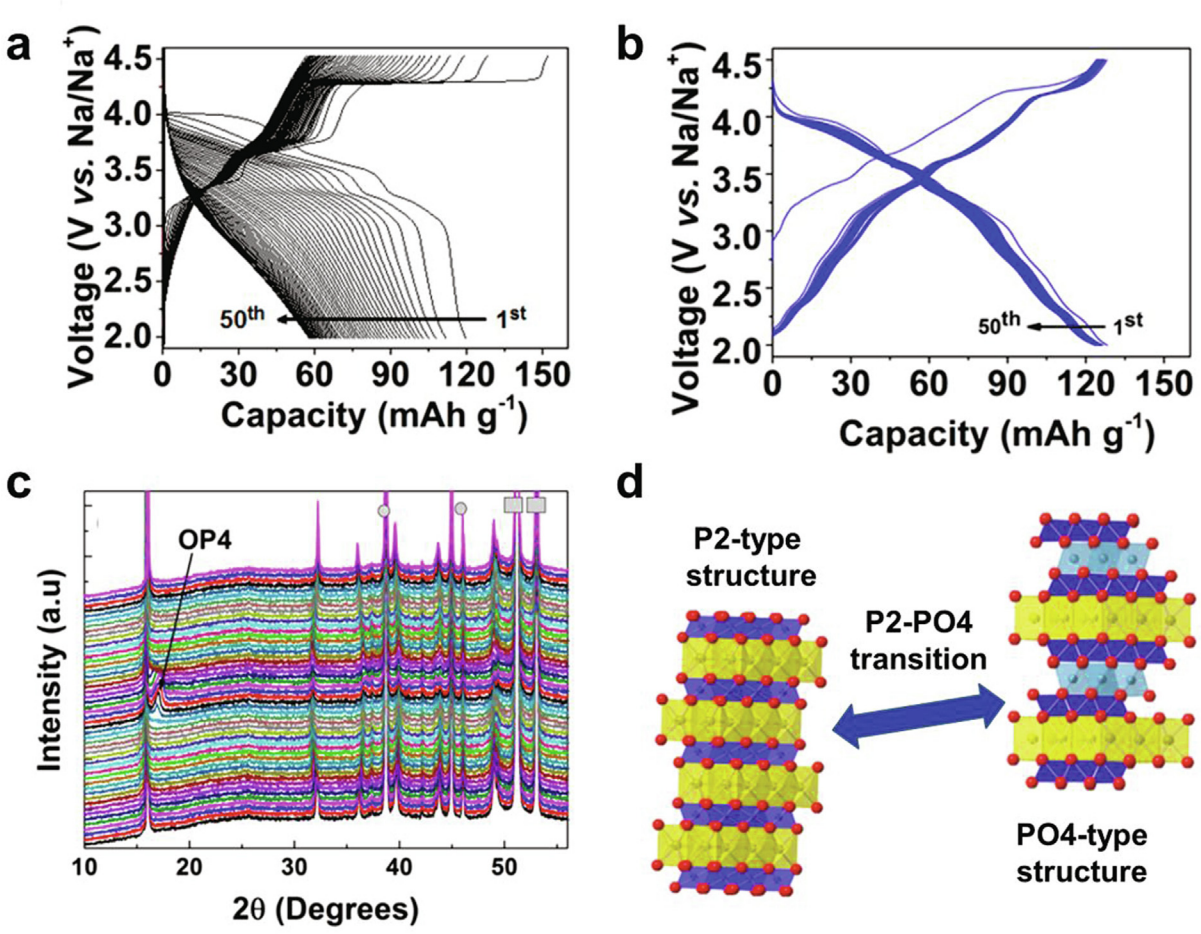

FIGURE 5

The charge/discharge curves of (a) $Na_{0.67}Mg_{0.1}Ni_{0.2}Mn_{0.7}O_2$ and (b) $Na_{0.67}Ni_{0.3}Mn_{0.7}O_2$ at different cycles. (c) The in-situ XRD patterns $Na_{0.67}Mg_{0.1}Ni_{0.2}Mn_{0.7}O_2$ showing P2-PO4 phase transition (■ and ● correspond to the peaks of Be window Al current collector, respectively). (d) The schematic illustration of P2-PO4 phase transition. Reproduced with permission from Ref. [40]. Copyright 2016, American Chemical Society.

Please cite this article in press as: F. Xiong et al., Materials Today, (2021), https://doi.org/10.1016/j.mattod.2020.12.002

(dashed red line) transfer through the external circuit to the Fermi level of cathode material (dashed blue line). Therefore, the relationship of open-circuit voltage and the chemical potentials of anode and cathode materials (μ_{anode} and $\mu_{cathode}$, respectively, i.e., their Fermi energies) can be described as [32–34]:

$$eV_{oc} = \mu_{anode} - \mu_{cathode} \quad (3)$$

where e is the magnitude of the electron charge. For many cathode materials, the positions of Fermi level are typically localized on the transition metal redox center. Therefore, substituting transition metal by another one can alter the chemical potential of cathode materials, thus the electrochemical potential.

Besides, the position of conduction-band states of cathode materials is directly related to the bonding characteristics of metal–ligand (MX) bond. With the increase of ionic contribution to the bonding, the separation between the bonding (σ) and antibonding (σ^*) orbitals will decrease (Fig. 2b). The downward shift of the lowest unoccupied 3d metal levels (σ^*) translates into a downward shift of the dashed blue line displayed in Fig. 2a, indicating the increased potential of cathode materials [33]. This is so called "the inductive effect", which has been confirmed in many polyanionic electrode materials. Based on this mechanism, it is possible to modify the potential of cathode materials by defects engineering which alters the bonding characteristics of the MX bonds.

Improving structural stability

The structural stability of cathode materials during the electrochemical process determines the cycling performance, while a lot of cathode materials suffer the poor structural stability. Therefore, improving the structural stability of cathode materials is significant for the practical application. The stress resulted from the volume change during the ion intercalation/deintercalation is one of the major reasons for the structural damage during the cycling process. Crystal defect modulation such as substitutional doping is able to reduce the volume change of cathode materials during the ion intercalation/deintercalation process, and thus improve the structural stability [35,36]. For layered cathode materials, the interstitial impurities in interlayer can act as pillars to enhance the stability of layered structure, which has come to be known as the "pillar effect" [37].

Except for the above roles, crystal defects in cathode materials also possess other functions, such as acting as intercalation sites, inhibiting harmful phase transition, suppressing dissolution and so forth, in some special cases. These will be summarized and discussed in the corresponding section. In summary, crystal defects in cathode materials are highly related to the physical and chemical properties and crystal defect modulation is an efficient way to adjust the electrochemical performance.

Crystal defect modulation in cathode materials for Non-Lithium ion batteries

Substitutional impurity

The impurities are classified to substituional and interstitial types. Substitutional impurity refers to the introduced impurity atom that replaces the original atom and occupies its lattice site, and interstitial impurity refers to the introduced impurity atom/ion that locates at previously unoccupied sites in the lattice. Similarly, doping, introducing impurity atom, are classified to substitutional and interstitial doping. For cathode materials, substitutional doping is mainly classified to substitutional cation doping and substitutional anion doping, also called as cation substitution and anion substitution, respectively. Here, we have summarized the recent progress of cation substitution and anion substitution in cathode materials for NLIBs (Table 1), respectively. The positive effects and mechanisms toward improved electrochemical performance are illustrated and discussed.

Cation substitution

Cation substitution might be the most successful crystal defect modulation strategy on cathode materials for metal-ion batteries as some LIBs cathode materials with cation substitution have now been commercialized, such as Li(Ni, Co, Mn)O_2, Li(Ni, Co, Al)O_2, $LiNi_{0.5}Mn_{1.5}O_4$, Li(Fe, Mn)PO_4. The effects of cation substitution are depended on the kinds of electrode materials and substitution ions. Generally, the effects of cation substitution on electrode materials mainly classified to three aspects: (1) kinetics improvement, (2) stability enhancement, and (3) potential modification. Here, we have highlighted some representative works to demonstrate those positive effects of cation substitution in different kinds of cathode materials for NLIBs.

Kinetics Improvement. Cation substitution has been widely used in the cathode materials for sodium-ion batteries (SIBs) to enhance the rate performance by improving kinetics properties, including electronic conductivity and ionic diffusivity. For the aliovalent substitution, some holes or electrons will generate to maintain electrical neutrality, which increases the electronic conductivity of cathode materials. Besides, the equivalent substitution can also enhance the electronic conductivity by tunning the band structure due to the different electron structure between doping ion and pristine ion. In addition, cation substitution may enlarge the ion diffusion channel, and reduce the strength of Na-O bond or change the sodium/vacancy (Na/V_{Na}) ordering, resulting in the increased ionic diffusivity.

P2-type layered oxide cathode materials for SIBs possess possible direct Na-ion diffusion channel because of that the prismatic sodium-ion sites are face-sharing. Thus, P2-type layered oxides are expected to display excellent rate performance. However, the rate performance of many reported P2-type layered oxides is far from expected due to that the Na/V_{Na} ordering may reduce the Na diffusivity by trapping vacancies. [89]. Cation substitution is an efficient approach to inhibit the Na/V_{Na} ordering thereby increasing the Na diffusivity. Bucher *et al.* reported that the substitution of Co for Mn in P2-Na_xMnO_2 successfully suppress the Na/V_{Na} ordering, which is the origination for the superior rate performance of P2-$Na_xCo_{0.1}Mn_{0.9}O_2$ compared to P2-Na_xMnO_2 [61]. Li et al. found that the introduction of Co into P2-type layered compound not only enhances the Na^+ diffusion kinetics but also increase the electronic conductivity [60]. However, Co element is toxic and expensive, thus selecting the non-toxic element to suppress Na/V_{Na} ordering is more economical. Recently, Guo and co-workers realized the Na/V_{Na} disordering in P2-$Na_{2/3}Ni_{1/3}Mn_{2/3}O_2$ by Ti-substitution (Fig. 3a) [50]. Ti-substitution increases the interaction between transition metal and oxygen and reduces the binding energy of Na-O bond, resulting in the expanded sodium layer and shrunk transition

Please cite this article in press as: F. Xiong et al., Materials Today, (2021), https://doi.org/10.1016/j.mattod.2020.12.002

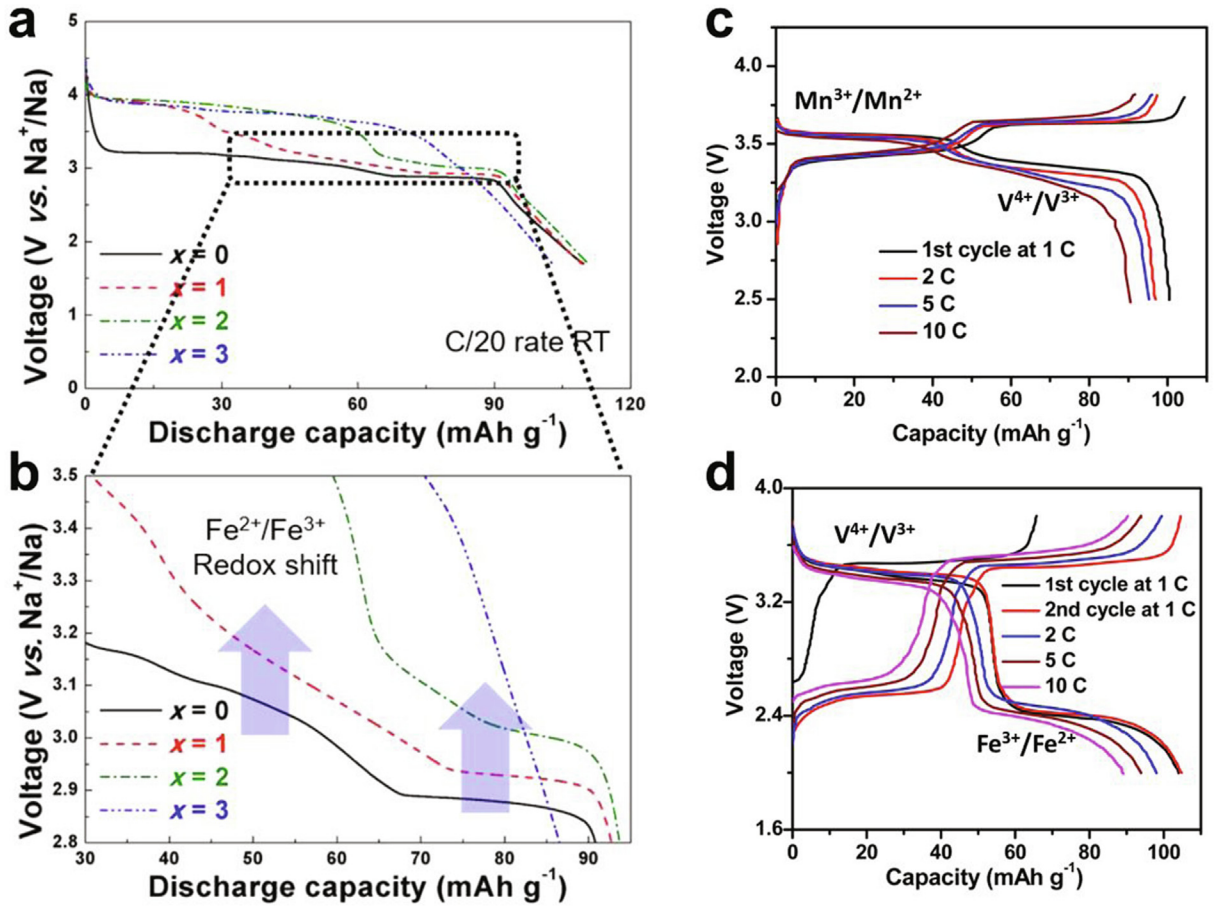

FIGURE 6

(a and b) The discharge curves of $Na_4Mn_xFe_{3-x}(PO_4)_2(P_2O_7)$ ($x = 0$, 1, 2 or 3). Reproduced with permission from Ref. [35]. Copyright 2016, American Chemical Society. The charge/discharge curves of (c) $Na_4MnV(PO_4)_3$ and (d) $Na_3FeV(PO_4)_3$. Reproduced with permission from Ref. [55]. Copyright 2016, American Chemical Society.

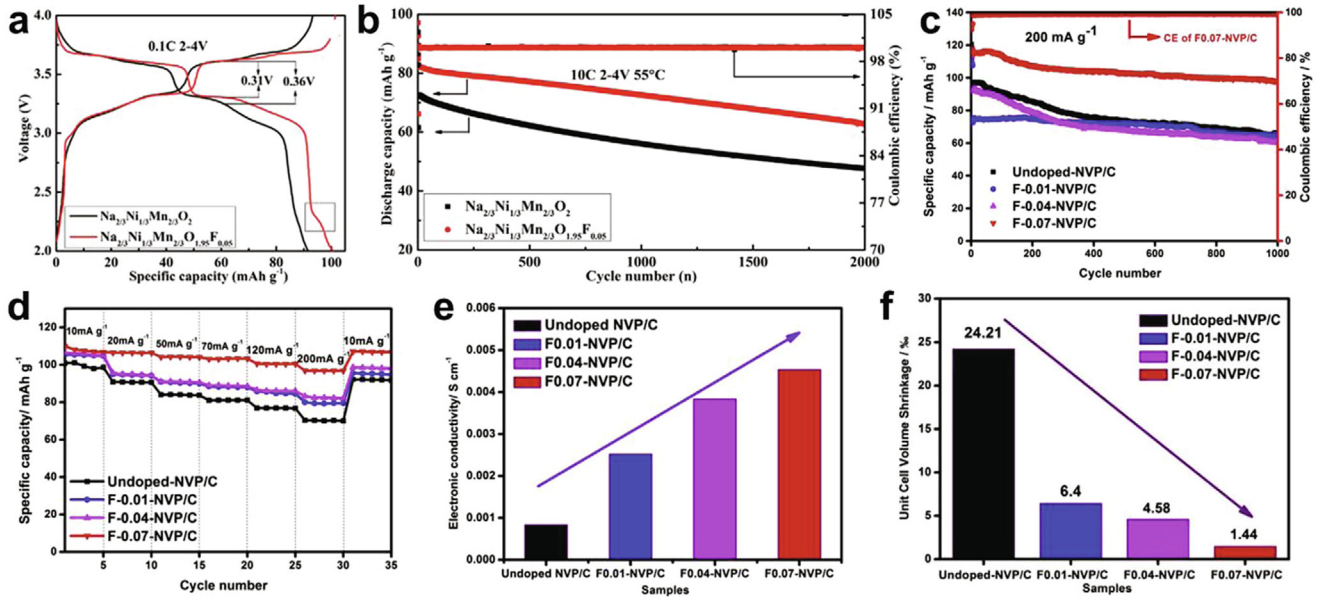

FIGURE 7

(a) The charge–discharge curves and (b) cycling stability of $Na_{2/3}Ni_{1/3}Mn_{2/3}O_2$ and $Na_{2/3}Ni_{1/3}Mn_{2/3}O_{1.95}F_{0.05}$. Reproduced with permission from Ref. [77]. Copyright 2020, WILEY-VCH Verlag GmbH & Co. KGaA, Weinheim. (c) The cycling performance, (d) rate capability, (e) electronic conductivity and (f) unit cell volume shrinkages of $Na_3V_2(PO_4)_{3-x}F_x/C$ ($x = 0$, 0.01, 0.04 and 0.07). Reproduced with permission from Ref. [36]. Copyright 2017, 2017 Elsevier B.V.

Please cite this article in press as: F. Xiong et al., Materials Today, (2021), https://doi.org/10.1016/j.mattod.2020.12.002

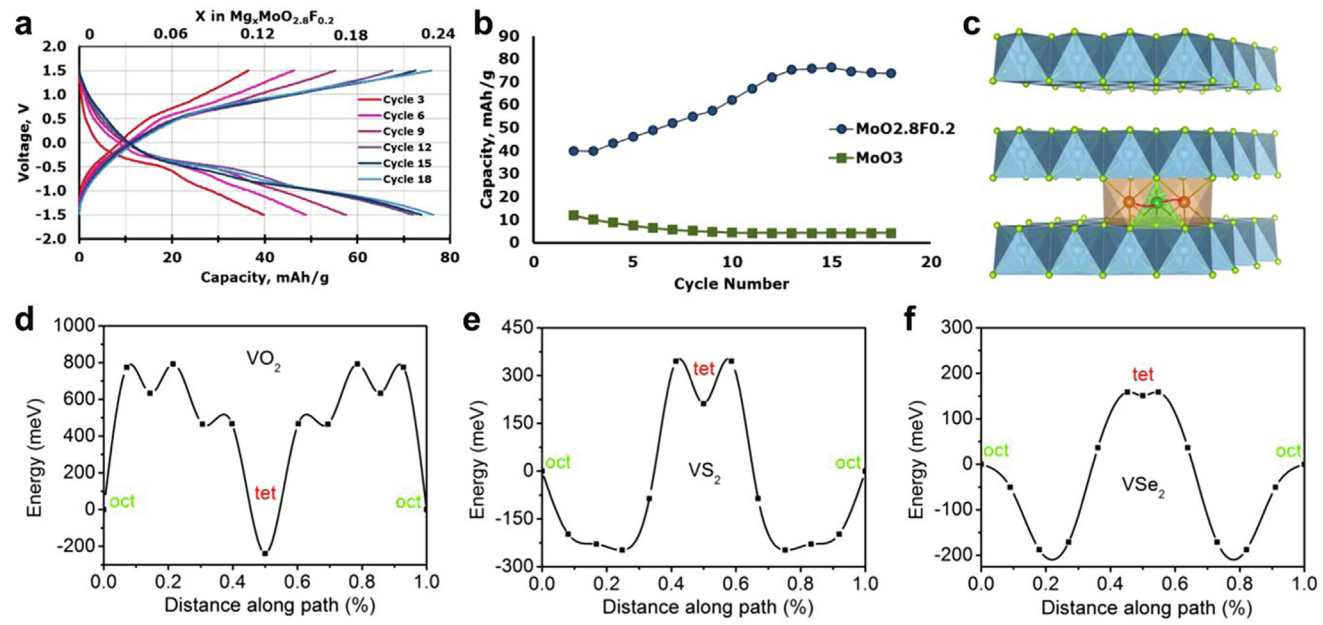

FIGURE 8

(a) The charge/discharge curves of $MoO_{2.8}F_{0.2}$ and (b) cycling performance of α MoO_3 and $MoO_{2.8}F_{0.2}$. Reproduced with permission from Ref. [83]. Copyright 2016, American Chemical Society. (c) Crystal structure of layered MX_2 (M = Ti, V; X = O, S, Se), and corresponding calculated diffusion energy barrier of Mg^{2+} in layered (b) VO_2, (c) VS_2, and (d) VSe_2. Reproduced with permission from Ref. [116]. Copyright 2019, American Chemical Society.

metal layers. The sodium/vacancy ordering is effectively suppressed due to the substantial difference in the Fermi level between Ti^{4+} and Mn^{4+}. The Ti-doped sample (P2-$Na_{2/3}Ni_{1/3}Mn_{1/3}Ti_{1/3}O_2$) with Na/V_{Na} disordering displays highly enhanced rate performance compared to P2-$Na_{2/3}Ni_{1/3}Mn_{2/3}O_2$ with sodium/vacancy ordering (Fig. 3b). The excellent rate performance is attributed to the Na/V_{Na} disordering which ensures the high Na diffusivity of 10^{-10} to 10^{-9} cm^2 s^{-1} and lower diffusion barrier of 170 meV (Fig. 3c). Besides, Zn [72], Mg [41] and Zr substitution [73] can also enhance the sodium-ion diffusion by suppressing the Na/V_{Na} ordering. Moreover, Mg substitution also has been applied in the layered cathode materials for potassium-ion batteries (PIBs) and displayed positive effect on K-ion diffusion [43].

Besides, cation substitution could create oxygen vacancies in some cases, which also has significant effect on the electron/ion transport kinetics of cathode materials. Lian et al. [52] reported that Ti substitution in MnO_2 would lead to the generation of oxygen vacancies, which open the [MnO_6] octahedral walls, facilitating the ion diffusion. Moreover, the Ti substitution and the oxygen vacancy will lead to imbalanced charge distribution and local electric field, which accelerate ion/electron migration rates in MnO_2. Due to the synergetic effects of Ti substitution and oxygen vacancy, the Ti-substituted MnO_2 exhibits enhanced rate capability when evaluated as cathode materials for zinc-ion batteries (ZIBs). Similarly, Cu substitution also creates oxygen vacancies in Mn_2O_3, resulting faster ion diffusion rate and better rate performance [71].

In addition, cation substitution has also been employed to modify the kinetics of polyanionic cathode materials for SIBs, especially $Na_3V_2(PO_4)_3$ [42,48,75,90] and $Na_3V_2(PO_4)_2F_3$ [51,54,74,76]. For instance, Yi et al. [51] investigated the electrochemical performance of Ti^{x+} ($x = 2$, 3, 4)-doped $Na_3V_2(PO_4)_2F_3$. The effect of doping amount on electrochemical performance of Ti-doped $Na_3V_2(PO_4)_2F_3$ was investigated, rendering that the sample with 5 mol% Ti doping achieves highest capacity. The moderate Ti-doping can enable the promoted electrical conduction and sodium-ion diffusion. According to the density functional theory (DFT) calculation, the Ti-doped $Na_3V_2(PO_4)_2F_3$ possesses reduced band gap compared with pristine $Na_3V_2(PO_4)_2F_3$ (Fig. 3d–f). Ti^{2+}-doped sample delivers the highest sodium diffusion coefficient and the smallest particle size at the same conditions. Consequently, the Ti^{2+}-doped $Na_3V_2(PO_4)_2F_3$ cathode exhibits the best rate performance. Even at the high rate of 40, 80 and 200C, the capacities of 104, 81, 41 mA h g^{-1} were still obtained, respectively.

Stability Enhancement. The cycling stability is highly relevant with the structural stability of electrode materials. The structural stabilities of some promising cathode materials are suffering from various issues, such as low thermal stability, dissolution and the detrimental phase transition during the electrochemical operation. Cation substitution doping can efficiently solve or alleviate these issues, then contributing to the enhanced cycling stability. On the other hand, the air stability of electrode materials is also an important property for practical application, which can also be modified by cation substitution doping.

The Ni-rich layered cathode materials possess high capacity but suffer from the insufficient thermal stability. The substitution of Co or Mn for Ni can improve thermal stability but inevitably sacrifice the capacity [91]. In order to reduce the capacity sacrifice after the ion substitution, Hwang et al. [62] designed the gradient substituted $Na[Ni_{0.60}Co_{0.05}Mn_{0.35}]O_2$ with varied composition from the inner to the outer (Fig. 4a–c). The substitution of Mn for Ni in outer shell enhances the thermal stability,

Please cite this article in press as: F. Xiong et al., Materials Today, (2021), https://doi.org/10.1016/j.mattod.2020.12.002

TABLE 2

Summary of electrochemical performance of cathode materials with interstitial impurity for NLIBs.

Interstitial Impurity	Materials	Battery system	Highest specific capacity/current density (mAh g^{-1}/mA g^{-1})	Average discharge potential (V)	Rate performance (mAh g^{-1}/mA g^{-1})	Cycling performance (mAh g^{-1}/*n*/mA g^{-1})	Ref.
Li^+	LiV_3O_8	MIBs	252.2/100	~1.75 *vs.* Mg^{2+}/Mg	–	106.4/30/100	[117]
Na^+	NaV_3O_8	MIBs	204.2/100	~1.75 *vs.* Mg^{2+}/Mg	62.4/1000	~175.0/100/100	
K^+	KV_3O_8	MIBs	37.6/100	~1.9 *vs.* Mg^{2+}/Mg	–	33.3/30/100	
Na^+	$Na_{0.33}V_2O_5$	ZIBs	276.6/200	~0.7 *vs.* Zn^{2+}/Zn	96.4/2000	218.4/1000/1000	[118]
Na^+	δ-$Na_xV_2O_5{\cdot}nH_2O$	ZIBs	374.9/100	~0.7 *vs.* Zn^{2+}/Zn	119.7/5000	264.8/4000/2000	[119]
K^+	δ-$K_{0.51}V_2O_5$	PIBs	131/30	3.2 *vs.* K^+/K	64/10000	45.6/100/4000	[120]
K^+	$K_{0.486}V_2O_5$	PIBs	159/20	~2.7 *vs.* K^+/K	12.8/1000	44.3/150/100	[121]
K^+	$K_xV_2O_5{\cdot}nH_2O$	PIBs	~265/~6	~2.8 *vs.* K^+/K	~130/300	167.24/50/~20	[122]
K^+	$KV_{12}O_{30\text{-}y}{\cdot}nH_2O$	ZIBs	436/50	~0.7 *vs.* Zn^{2+}/Zn	227/10000	300/3000/5000	[123]
K^+	$K_{0.5}V_2O_5$	ZIBs	436.2/500	~0.7 *vs.* Zn^{2+}/Zn	188.9/5000	140.3/3000/5000	[124]
K^+	$K_{0.19}MnO_2$	ZIBs	270/308	~1.3 *vs.* Zn^{2+}/Zn	113/6160	180/400/1540	[125]
Mg^{2+}	$Mg_{0.3}V_2O_5{\cdot}1.1H_2O$	MIBs	164/100	~2.2 *vs.* Mg^{2+}/Mg	50/4000	108/10000/1000	[126]
Mg^{2+}	$Mg_{0.34}V_2O_5{\cdot}0.84H_2O$	ZIBs	~353/50	~0.75 *vs.* Zn^{2+}/Zn	81/5000	~85/2000/5000	[127]
Mg^{2+}	$Mg_{0.25}V_2O_5{\cdot}H_2O$	CIBs	~120/20	~0.9 *vs.* Ca^{2+}/Ca	70.2/100	61/500/100	[128]
Ca^{2+}	$Ca_{0.25}V_2O_5{\cdot}nH_2O$	ZIBs	340/60	~0.9 *vs.* Zn^{2+}/Zn	72/24000	~55/5000/24000	[129]
Ca^{2+}	$Ca_{0.13}MoO_3{\cdot}0.41H_2O$	CIBs	192/86	2.4 *vs.* Ca^{2+}/Ca	109/342.6	85.3/50/342.6	[130]
Ca^{2+}	$Ca_{0.28}MnO_2{\cdot}0.5H_2O$	ZIBs	298/175	~1.35 *vs.* Zn^{2+}/Zn	124.5/3500	100.9/5000/3500	[131]
Fe^{3+}/Fe^{2+}	Fe-VO_x	SIBs	184/100	~2.0 *vs.* Na^+/Na	92/2000	147.2/50/100	[132]
Ni^{2+}	δ-$Ni_{0.25}V_2O_5{\cdot}nH_2O$	ZIBs	402/200	~0.7 *vs.* Zn^{2+}/Zn	147/5000	213.6/1200/5000	[133]
Mn^{2+}	$Mn_xV_2O_5A_y{\cdot}nH_2O$	ZIBs	415/50	~0.7 *vs.* Zn^{2+}/Zn	214/8000	260/2000/4000	[134]
Mn^{2+}	$Mn_{0.04}V_2O_5{\cdot}1.17H_2O$	MIBs	145/50	~2.2 *vs.* Mg^{2+}/Mg	50/4000	79.7/10000/2000	[135]
Zn^{2+}	$Zn_{0.25}V_2O_5{\cdot}nH_2O$	ZIBs	282/300	~0.75 *vs.* Zn^{2+}/Zn	183/6000	210/1000/2400	[136]
Y^{3+}	$Y_{0.02}V_2O_5{\cdot}nH_2O$	SIBs	180/100	~1.75 *vs.* Na^+/Na	-	119/100/100	[137]

and the inner with high Ni content exhibits high capacity. Consequently, the gradient substituted $Na[Ni_{0.60}Co_{0.05}Mn_{0.35}]O_2$ displays enhanced cycling stability at elevated temperature (Fig. 4d). After cycling for 100 cycles at 55 °C, the gradient substituted $Na[Ni_{0.60}Co_{0.05}Mn_{0.35}]O_2$ displays the capacity of 98.0 mA h g^{-1}, which is much higher than that of $Na[Ni_{0.60}Co_{0.05}Mn_{0.35}]O_2$ without gradient substitution (below 20 mA h g^{-1}). The differential scanning calorimetry (DSC) results demonstrate that the exothermic peak of desodiated gradient substituted $Na[Ni_{0.60}Co_{0.05}Mn_{0.35}]O_2$ appeared at lower temperature (293.5 °C) and displayed less heat release (172 J g^{-1}) compared to bulk one without gradient substitution (266.5 °C, 321.6 J g^{-1}), demonstrating the improved thermal stability and safety of gradient substituted sample.

For some layered cathode materials, the harmful phase transition always occurs at high voltage, resulting in the fast capacity decay. The metal-site substitution is identified as an efficient way to improve cycling stability by restraining the harmful phase transition. For example, the P2-O2 phase transition commonly appears in P2-type layered oxide cathode at highly charge state (over 4.2 V), especially in Na-Ni-Mn-O system. Cation substitution doping, including Li [92] Mg [39,40] Ti [93] Fe [94,95] Co [96] Cu [67] and Zn [72] doping, can effectively suppressed or transferred this detrimental phase transition to more reversible P2–OP4 evolution [18]. For instance, Singh et al. [40] reported the Mg-substituted P2-$Na_{0.67}Ni_{0.3-x}Mg_xMn_{0.7}O_2$ ($x = 0.05,\ 0.1$) as cathode materials for SIBs. Compared with pristine P2-$Na_{0.67}Ni_{0.3}Mn_{0.7}O_2$, the Mg-substituted cathode displays improved cycling performance and rate capability (Fig. 5a and b). According to the *in-situ* X-ray diffraction (XRD), the P2-O2 phase transition occurs in the P2-$Na_{0.67}Ni_{0.3}Mn_{0.7}O_2$ at ~4.25 V, whereas the O2 phase is absent for P2-$Na_{0.67}Ni_{0.2}Mg_{0.1}Mn_{0.7}O_2$ (Fig. 5c) and the characteristic peak of OP4 phase was observed in 4.2–4.5 V. Thus, Mg substitution suppresses the P2-O2 transition and transfers it as P2-OP4 transition, leading to superior cycling stability (Fig. 5d).

Recently, the strategy of activating anionic redox (O^{2-}/O_n^-) has been applied in layered SIBs cathode materials so as to improve the energy density [97–99]. However, the development of cathode materials with activated oxygen redox is suffering from poor cycling stability due to the irreversible oxygen loss (O_2 release) [97–100]. Increasing the orbital interaction between metal and oxygen by cation substitution has been demonstrated as an efficient way to suppress the oxygen loss [45,46,57,101,102]. For example, Huang et al. [57] confirmed that the oxygen release in $Na_{2/3}Ni_{1/3}Mn_{2/3}O_2$ can be efficiently suppressed by the partial substitution of Mn by Fe. That is attributed to that the formation of high covalent binding Fe–(O–O) bonding. Therefore, $Na_{2/3}Fe_{2/9}Ni_{2/9}Mn_{5/9}O_2$ exhibited highly promoted cycling stability compared to $Na_{2/3}Ni_{1/3}Mn_{2/3}O_2$. In addition, the partially substituting of 3d metals by 4d or 5d metals is feasible to suppress the oxygen loss owing to the larger orbital interaction between 4d/5d metals wtih oxygen compared to that of 3d metal with oxygen [99]. For example, Zhou et al. [101] confirmed that the partial substitution of Mn by 5d metal Ir in $Na_{1.2}Mn_{0.4}Ir_{0.4}O_2$ can efficiently suppress the oxygen loss in Na-rich Mn-based materials by forming strong covalent TM-O bond. Moreover, they also reported that the oxygen loss in P2-$Na_{0.66}Li_{0.22}Mn_{0.78}O_2$ can be efficiently suppressed by Ti substitution [103]. Meanwhile, the Mn-related Jahn–Teller distor-

Please cite this article in press as: F. Xiong et al., Materials Today, (2021), https://doi.org/10.1016/j.mattod.2020.12.002

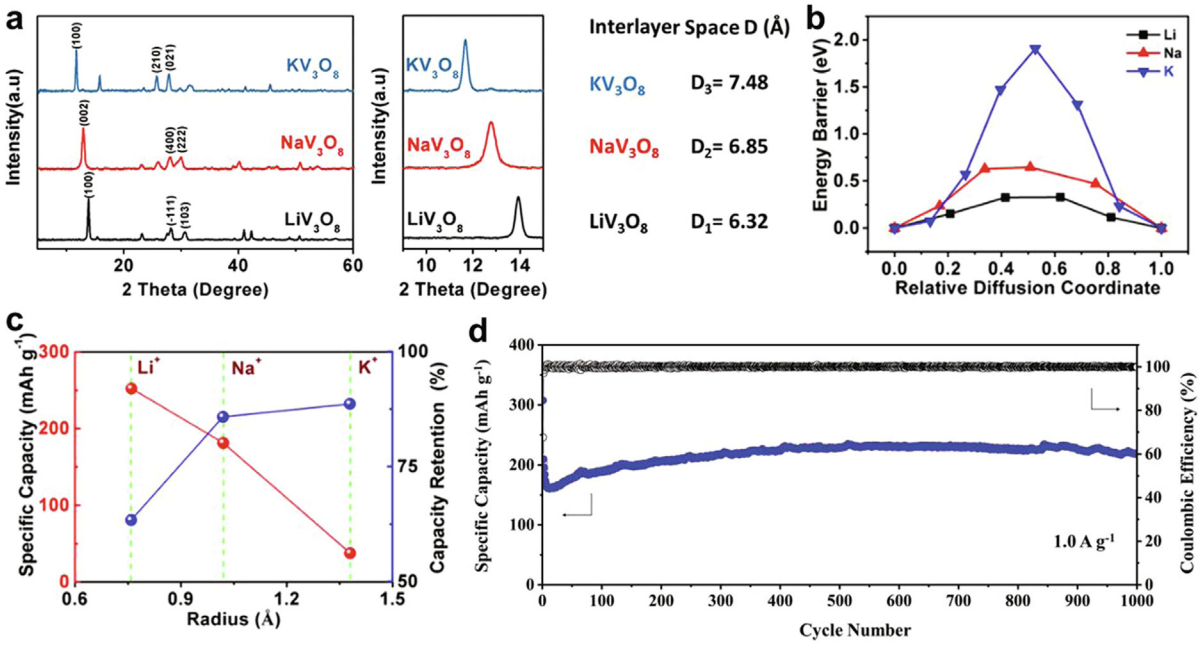

FIGURE 9

(a) The XRD patterns of A-V_3O_8 (A = Li, Na, K), (b) the diffusion energy barriers of pre-intercalated alkali metal ion in A-V_3O_8 (A = Li, Na, K); (c) The specific capacity and capacity retention of A-V_3O_8 (A = Li, Na, K); Reproduced with permission from Ref. [117]. Copyright 2019, Elsevier Ltd. (d) The cycling performance of $Na_{0.33}V_2O_5$ as cathode materials for ZIBs. Reproduced with permission from Ref. [118]. Copyright 2018, WILEY-VCH Verlag GmbH & Co. KGaA, Weinheim.

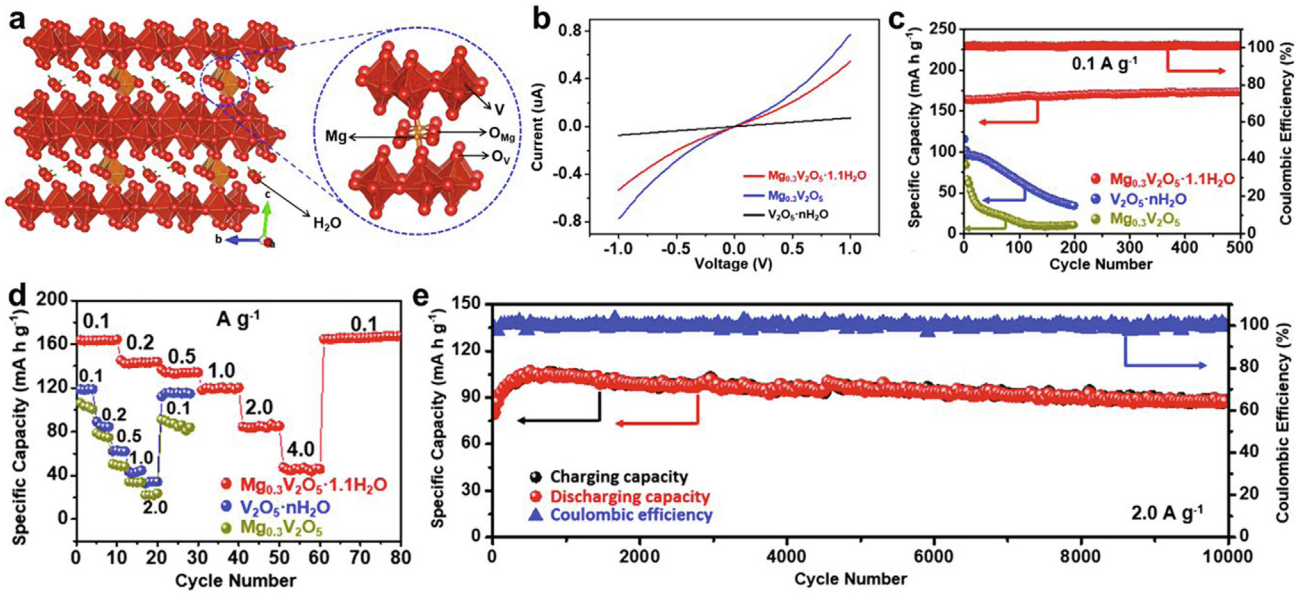

FIGURE 10

(a) The structural illustration of Mg-ion pre-intercalated bilayered V_2O_5 ($Mg_{0.3}V_2O_5{\cdot}1.1H_2O$); (b) I–V plots, (c) cycling stability and (d) rate capability of $Mg_{0.3}V_2O_5{\cdot}1.1H_2O$, $V_2O_5{\cdot}1.1H_2O$ and $Mg_{0.3}V_2O_5$; (e) Long-term cycling performance of $Mg_{0.3}V_2O_5{\cdot}1.1H_2O$. Reproduced with permission from Ref. [126]. Copyright 2019, Elsevier Inc.

tion in Ti substituted P2-$Na_{0.66}Li_{0.22}Mn_{0.78}O_2$ ($Na_{0.66}Li_{0.22}Ti_{0.15}Mn_{0.63}O_2$) was restrained. Consequently, the remarkably enhanced cycling stability was obtained in $Na_{0.66}Li_{0.22}Ti_{0.15}Mn_{0.63}O_2$ compared to Ti-free one. Unfortunately, the work mechanism of Ti substitution on suppressing oxygen loss is still ambiguous, which needs further work to unravel.

Cation substitution also has been employed to modify the cycling stability of cathode materials for PIBs. For Mn-based layered cathode materials, the cycling performance is suffering from the structural deterioration resulted from the Jahn–Teller effects of Mn^{3+} [44,56,66]. Some recent investigations confirm that cation substitution is an efficient strategy to improve the cycling

Please cite this article in press as: F. Xiong et al., Materials Today, (2021), https://doi.org/10.1016/j.mattod.2020.12.002

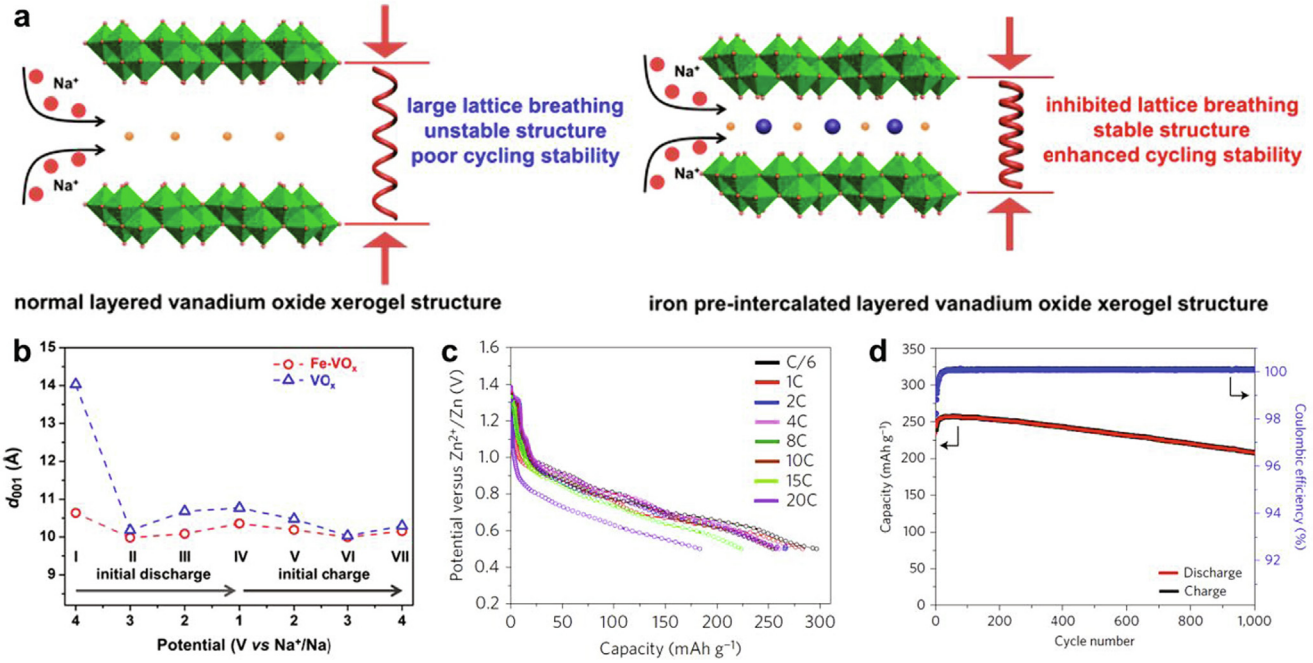

FIGURE 11

(a) The schematic illustration for large lattice breathing in pristine vanadium oxide xerogel and inhibited lattice breathing in iron pre-intercalated vanadium oxide xerogel; (b) The interlayer spacing evolution of pristine and iron pre-intercalated vanadium oxide xerogel during the first discharge/charge process. Reproduced with permission from Ref. [132]. Copyright 2015, American Chemical Society. (c) The discharge curves at different rates and (d) cycling performance at 2400 mA g^{-1} of $Zn_{0.25}V_2O_5{\cdot}nH_2O$ as cathode material for ZIBs; Reproduced with permission from Ref. [136]. Copyright 2016, Macmillan Publishers Limited, part of Springer Nature.

stability of Mn-based layered cathode materials for PIBs by suppressing the Jahn–Teller effects and alleviating the structural degradation. Bai et al. [66] reported the partial substitution of Mn by Ni in $K_{0.67}MnO_2$ would remarkably enhance the rate performance and cycling stability. The refined XRD results indicate that the Jahn-Teller effects are effectively suppressed in Ni substituted $K_{0.67}MnO_2$ ($K_{0.67}Mn_{0.83}Ni_{0.17}O_2$) compared to pristine one, which is responsible for the improved electrochemical performance. In addition, Mg/Al substitution in $K_{0.45}Ni_{0.1}Co_{0.1}Mn_{0.8}O_2$ also can effectively alleviate the Jahn-Teller distortion [44].

In addition, the air stability is one issue that needs to be solved for many layered oxide cathode materials for SIBs, such as O3-$NaNi_{0.5}Mn_{0.5}O_2$ [104], P2-$Na_{2/3}Fe_{1/2}Mn_{1/2}O_2$ [105], and P2-$Na_{2/3}Mn_{1/3}Fe_{1/3}Co_{1/3}O_2$ [106]. At present, the investigations about improving the air stability are still in the early stage. Recently, some Cu-substituted layered oxides display enhanced air stability [59,68,107]. Yao et al. [107] presented the Cu/Ti co-substituted $NaNi_{0.45}Cu_{0.05}Mn_{0.4}Ti_{0.1}O_2$ cathode, which displays an 20 times increased stable air-exposure period and maintains its pristine structure and capacity after soaking in water.

Potential Modification. Apart from the specific capacity, the energy density of battery is also determined by the working voltage which is depended on the equilibrium potential gap between cathode and anode. The potential of electrode materials with similar structure is mainly determined by the redox couple. Thus, introducing the redox couple with higher potential into cathode materials by cation substitution can improve the work voltage and the energy density of batteries.

$Na_4Fe_3(PO_4)_2(P_2O_7)$ is identified as an promising cathode materials due to its abundant resource, low cost, environmental friendliness, high stability and relatively high energy density compared to other Fe-based phosphates [108,109]. However, the relative low potential (3.2 V *vs*. Na^+/Na) based on Fe^{3+}/Fe^{2+} redox couples restrains its energy density. The framework of $Na_4Fe_3(PO_4)_2(P_2O_7)$ can be maintained after replacing Fe by other active metal, such as Mn, Co, and Ni. Based on the different active redox couples, $Na_4Mn_3(PO_4)_2(P_2O_7)$, $Na_4Co_3(PO_4)_2(P_2O_7)$ and $Na_4Ni_3(PO_4)_2(P_2O_7)$ display different potential of 3.8, 4.5 and 4.8 V (*vs*. Na^+/Na), respectively [110–112]. Due to the limited stability of the organic electrolyte, the most capacities of $Na_4Co_3(PO_4)_2(P_2O_7)$ and $Na_4Ni_3(PO_4)_2(P_2O_7)$ cannot be achievable before the decompose of electrolyte. Although the $Na_4Mn_3(PO_4)_2(P_2O_7)$ delivers higher potential and theoretical energy density compared to $Na_4Fe_3(PO_4)_2(P_2O_7)$, its development was restrained by the poor cycling stability resulted from the dissolution of Mn [110]. The Mn dissolution issue of Mn-based electrode materials has been mainly attributed to the disproportionation reaction of Mn(III). Therefore, the Mn(III) in charged $Na_4Mn_3(PO_4)_2(P_2O_7)$ may be responsible for the dissolution of Mn and the poor cycling stability [113]. Partially replacing Fe by Mn can improve the average potential of $Na_4Fe_3(PO_4)_2(P_2O_7)$ and maintain the good cycling stability simultaneously. Kim et al. reported the $Na_4Fe_3(PO_4)_2(P_2O_7)$ with different Mn-substitution content, i.e., $Na_4Mn_xFe_{3-x}(PO_4)_2(P_2O_7)$ ($x = 0$, 1, 2 or 3) [35]. The discharge curves of $Na_4Mn_xFe_{3-x}(PO_4)_2(P_2O_7)$ ($x = 0$, 1, 2 or 3) are shown in Fig. 6a and b, the plateaus at ~3.2 and ~3.8 V

Please cite this article in press as: F. Xiong et al., Materials Today, (2021), https://doi.org/10.1016/j.mattod.2020.12.002

TABLE 3

Summary of electrochemical performance of cathode materials with vacancy defect for NLIBs.

Vacancy type	Materials	Battery system	Highest specific capacity/current density (mAh g^{-1}/mA g^{-1})	Average discharge potential (V)	Rate performance (mAh g^{-1}/mA g^{-1})	Cycling performance (mAh g^{-1}/*n*/mA g^{-1})	Ref.
Mn	$Na_{4/7-x}[\square_{1/7}Mn_{6/7}]O_2$	SIBs	~200/8.3	~2.7 vs. Na^+/Na	–	~170/20/8.3	[142]
Mn	$Na_{4/7}[\square_{1/7}Mn_{6/7}]O_2$	SIBs	~220/–	~2.7 vs. Na^+/Na	–	~108/45/–	[143]
Mn	$Na_{1.8}Mn[Fe(CN)_6]_{0.88}[\square, Fe(CN)_6]_{0.12}\cdot 2.65H_2O$	SIBs	134/25	~3.2 vs. Na^+/Na	–	83.1/2700/500	[144]
Mn	$Mn_{0.61}\square_{0.39}O$	ZIBs	300/100	~1.3 vs. Zn^{2+}/Zn	105/2000	116/1500/1000	[145]
Mn	$ZnMn_2O_4$	ZIBs	150/50	1.35 vs. Zn^{2+}/Zn	72/2000	~84.6/500/500	[146]
Ti	$Ti_{0.91}O_{1.64}(OH)_{0.36}$	MIBs	165.3/20	~0.5 *vs.* Mg^{2+}/Mg	48.6/1000	~100/200/100	[147]
Ti	$Ti_{0.78}\square_{0.22}O_{1.12}F_{0.40}(OH)_{0.48}$	MIBs	165/20	~0.5 *vs.* Mg^{2+}/Mg	~75/300	~65/500/300	[148]
		AIBs	120/20	~0.4 *vs.* Al^{3+}/Al	–	–	
O	Oc_u-Mn_2O_3	ZIBs	246/50	~1.4 *vs.* Zn^{2+}/Zn	62/5000	98.6/600/1000	[71]
O	black TiO_{2-x}	MIBs	147/50	~0.5 *vs.* Mg^{2+}/Mg	106/300	77/400/300	[149]
O	$VO_{1.75}$ (B)	ZIBs	375/100	~0.75 *vs.* Zn^{2+}/Zn	220/5000	175/2000/5000	[150]
O	VO_{2-x} (B)/graphene	ZIBs	370/100	~0.75 *vs.* Zn^{2+}/Zn	116/20000	186/5000/10000	[151]
O	V_6O_{13}	ZIBs	410/200	~0.75 *vs.* Zn^{2+}/Zn	223/5000	398/200/200	[152]
O	$V_6O_{13-\delta}$/C	ZIBs	~410/200	~0.75 *vs.* Zn^{2+}/Zn	~290/15000	~310/2000/10000	[153]
O	$K_2V_8O_{21-x}$	ZIBs	385/200	~0.7 *vs.* Zn^{2+}/Zn	166/20000	245/1000/3000	[154]
O	σ-MnO_2	ZIBs	345/200	~1.35 vs. Zn^{2+}/Zn	~70/30000	100.8/2000/5000	[155]
O	$K_{0.8}Mn_8O_{16}$	ZIBs	320/100	~1.35 vs. Zn^{2+}/Zn	~100/2000	~160/1000/1000	[156]
O	WO_{3-x}	AIBs	120/100	~0.5 *vs.* Al^{3+}/Al	–	~60/100/100	[157]
O	MoO_{3-x}	SIBs	156/100	~1.6 vs. Na^+/Na	79.2/1000	156.3/200/100	[158]
O	$NaMnO_{2-y-\delta}(OH)_{2y}$	SIBs	211.9/48.6	~3.0 vs. Na^+/Na	156/12150	173.8/100/2430	[159]
O	P-MnO_{2-x}	ZIBs	302.8/500	~1.35 vs. Zn^{2+}/Zn	150.1/10000	185.8/1000/3000	[160]
O	N-doped MnO_{2-x}	ZIBs	286.3/200	~1.35 vs. Zn^{2+}/Zn	121.5/3000	172.7/1000/1000	[88]

(*vs.* Na^+/Na) are corresponded to the Fe^{3+}/Fe^{2+} and Mn^{3+}/Mn^{2+} redox couples, respectively. With the increase of Mn-substitution content, the plateau at~3.8 V gradually lengthen and the potential of Fe^{3+}/Fe^{2+} redox couples were slightly improved, resulting in the improvement of average potential. The increased potential of Fe^{3+}/Fe^{2+} redox is ascribed to the increased average Fe–O bond length. In addition, $Na_4MnFe_2(PO_4)_2(P_2O_7)$ and $Na_4Mn_2Fe(PO_4)_2(P_2O_7)$ still displays excellent cycling stability.

The cation substitution could also apply in the bimetal Na^+ super ionic conductor (NASICON)-type cathode materials along with the potential modification. For example, Goodenough and co-workers investigated the electrochemical behavior of $Na_xMV(PO_4)_3$ (M = Mn, Fe, Ni) as cathode materials for SIBs [55]. Unlike the single discharge plateau of $Na_3V_2(PO_4)_3$, both $Na_4MnV(PO_4)_3$ and $Na_3FeV(PO_4)_3$ displays two discharge plateaus (Fig. 6c and d). The discharge plateaus located at 3.6, 3.3 and 2.4 V can be assigned to the Mn^{3+}/Mn^{2+}, V^{4+}/V^{3+}, and Fe^{3+}/Fe^{2+} redox couples, respectively.

The suitable cation substitution can efficiently eliminate or alleviate various drawbacks of electrode materials, improving the energy density, rate performance and cycling stability. However, the investigation of cation substitution in some new fields, such as improving air stability, is still at an outset stage and some improvement mechanisms are still unclear. The gradient substitution holds high promising to reduce substitution content without the decrease of the improvement, reducing the adverse impact of substitution cation. In future, some complex and novel cation substituted structure may be designed to realize multiple effects. Besides, the application of cation substitution in the electrode materials for PIBs and multivalent-ion batteries, still has long way to go.

Anion substitution

Except for cation substitution, anion substitution in cathode materials also possesses ability to improve electrochemical performance. However, the investigation about anion substitution in cathode materials for NLIBs are relative rare compared to that of cation substitution. Up to now, the investigations of anion substitution in cathode materials mainly focus on the fluorine substitution to oxygen and selenium substitution to sulfur. The differences in electronegativity and charge number of O and F leads to that the properties of F-substituted electrode materials significantly change. The selenium substitution is mainly applied in the sulfide cathode materials for magnesium-ion batteries (MIBs) to reduce the interaction between host and Mg-ions by utilizing the weaker electronegativity of Se^{2-} compared to S^{2-}.

Huang and co-worker first investigated the effect of fluorine substitution on the electrochemical performance of O3-type layered SIBs cathode material [79]. The O3-type layered cathode material with different fluorine substitution content were obtained and the O3-$NaNi_{1/3}Fe_{1/3}Mn_{1/3}O_{2-x}F_x$ ($x = 0.01$) displays the best rate performance and cycling stability. The enhanced electrochemical performance of O3-$NaNi_{1/3}Fe_{1/3}Mn_{1/3}O_{2-x}F_x$ ($x = 0.01$) is ascribed to that the suitable fluorine substitution suppresses the Jahn-Teller effect of Mn^{3+} and enhances the sodium-ion diffusion. After that, fluorine substitution has also been applied to some other layered cathode materials for SIBs, such as, $Na_{0.67}Li_{0.1}Fe_{0.4}Mn_{0.5}O_2$ [78], $Na_{0.6}Mn_{0.95}Ni_{0.05}O_2$ [114],

Please cite this article in press as: F. Xiong et al., Materials Today, (2021), https://doi.org/10.1016/j.mattod.2020.12.002

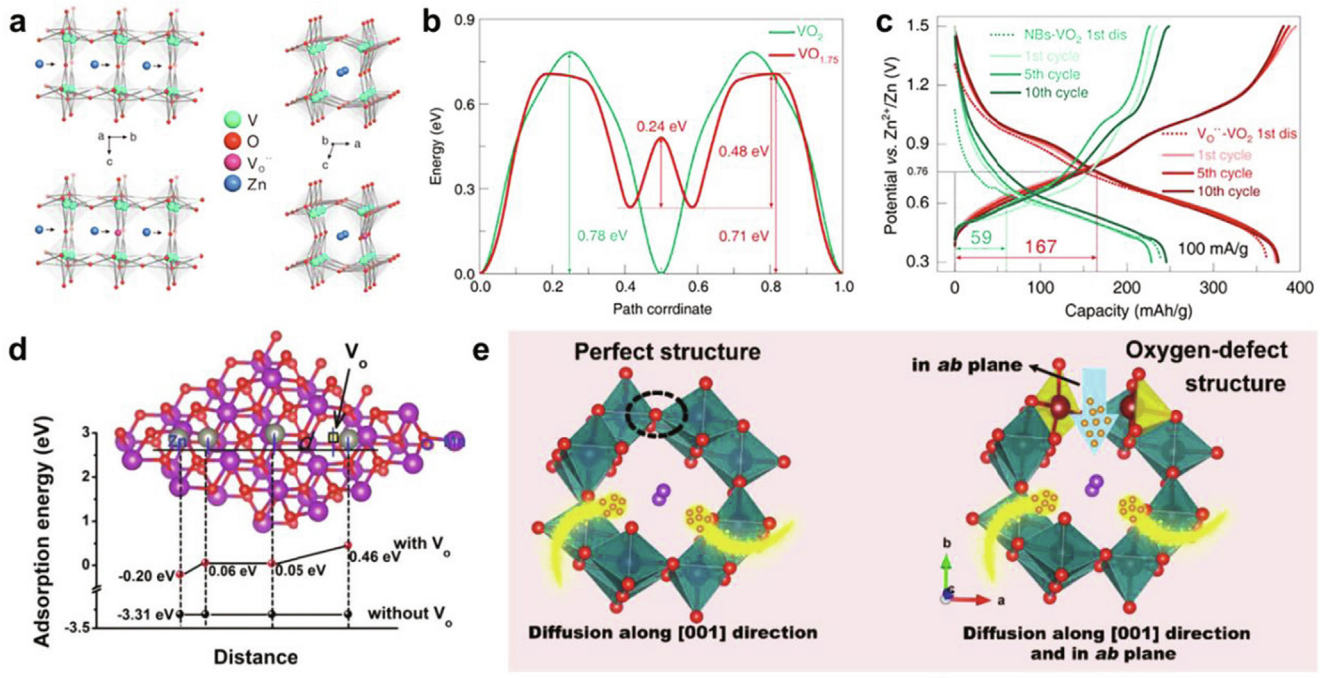

FIGURE 12

(a) The crystal structure, zinc ions diffusion pathways, (b) calculated zinc ions diffusion energy barrier, and (c) charge/discharge curves of VO_2 and oxygen vacancy-rich VO_2 ($VO_{1.75}$) as cathode materials for ZIBs. Reproduced with permission from Ref. [150]. Copyright 2020, American Chemical Society. (d) The calculated Zn^{2+} adsorption energies on the surfaces of less defective and oxygen-deficient σ-MnO_2. Reproduced with permission from Ref. [155]. Copyright 2019, WILEY-VCH Verlag GmbH & Co. KGaA, Weinheim. (e) Schematic illustration of ion diffusion in prefect and oxygen-deficient potassium manganate with 2 × 2 tunnels. Reproduced with permission from Ref. [156]. Copyright 2019, WILEY-VCH Verlag GmbH & Co. KGaA, Weinheim.

$Na_{0.65}Mn_{0.75}Ni_{0.25}O_2$ [80], and $Na_{2/3}Ni_{1/3}Mn_{2/3}O_2$ [77]. Recently, Liu et al. reported the F-substituted $Na_{2/3}Ni_{1/3}Mn_{2/3}O_2$ and investigated the effect of fluorine substitution on electrochemical behavior in detail [77]. According to the X-ray absorption near edge structure (XANES) spectroscopy and electron energy loss spectroscopy (EELS) results, the fluorine substitution partially reduced the Mn^{4+} to Mn^{3+}, and the electrochemically active Mn^{3+} is the origin for the increased capacity (Fig. 7a). Moreover, the operando XRD experiments demonstrate that the two-phase reaction in low-voltage region was suppressed by fluorine substitution. That is attributed to that the fluorine substitution increases the disorder of transition metal layer and breaks the cooperative Jahn–Teller effect. Consequently, $Na_{2/3}Ni_{1/3}Mn_{2/3}O_{1.95}F_{0.05}$ exhibited outstanding cycling performance. After 2000 cycles at 10 C and 55 °C, the capacity retention of 75.6% was obtained (Fig. 7b).

In addition, fluorine substitution has also been utilized to enhance the electrochemical performance of polyanionic cathode materials for SIBs [36,81,82]. Chen et al. [36] reported the enhanced rate capability and cycling stability of F-doped $Na_3V_2(PO_4)_3$ cathode (Fig. 7c and d). The $Na_3V_2(PO_4)_{2.93}F_{0.07}$/C composite displays a capacity of 97.8 mAh g^{-1} at 200 mA g^{-1} after 1000 cycles, whereas the capacity of undoped $Na_3V_2(PO_4)_3$/C composite at same condition is only 65.2 mAh g^{-1}. The improved electronic conductivity, diffusion kinetics and structure stability of F-doped $Na_3V_2(PO_4)_3$ compared to undoped one were demonstrated (Fig. 7e and f), which is responsible for the enhanced sodium storage performance. Recently, fluorophosphates receive significant attention due to their higher operating potential compared to phosphate counterparts. However, most fluorophosphates, such as $NaVPO_4F$, $Na_3V_2(PO_4)_2F_3$, $Na_3V_2O_2(PO_4)_2F$ and Na_2FePO_4F, will not be classified to F-substituted compounds in this review due to the large difference on crystal structure between them and their phosphate counterparts.

Except for cathode materials for SIBs, fluorine substitution has also been employed to the cathode materials for MIBs. For example, Incorvati et al. reported the electrochemical performance of F-substituted α-MoO_3 ($MoO_{2.8}F_{0.2}$) in MIBs [83]. Compared to undoped α-MoO_3, $MoO_{2.8}F_{0.2}$ delivered a significantly improved reversible magnesium storage capacity (Fig. 8a and b). Where after, Wan et al. investigated the role of fluorine substitution on magnesium storage behaviors of α-MoO_3 [115]. The DFT calculation demonstrated that the fluorine substitution reduces the diffusion energy barrier of Mg^{2+}, resulting in the improved magnesium storage performance of $MoO_{2.8}F_{0.2}$.

For MIBs, the strong interaction between divalent Mg^{2+} and anions of host lattice results in slow magnesium diffusion, which is a big obstacle for obtaining high-performance cathode materials for MIBs. Substituting anions of host lattice by less electronegative one is effective strategy to reduce this interaction and enhance the magnesium diffusion. Aurbach et al. first demonstrated that the Se-substituted $Mg_xMo_6S_8$ ($Mg_xMo_6S_7Se$ and $Mg_xMo_6S_6Se_2$) exhibited enhanced capacity and rate performance compared to pure $Mg_xMo_6S_8$ [85]. Recently, Wang and coworkers systematically investigated the effects of different anion (O, S, and Se) on magnesium-ion diffusion in layered MX_2 (M = Ti, V; X = O, S, Se) [116]. The DFT calculation results displayed that the activation barriers of Mg^{2+} diffusion in layered

Please cite this article in press as: F. Xiong et al., Materials Today, (2021), https://doi.org/10.1016/j.mattod.2020.12.002

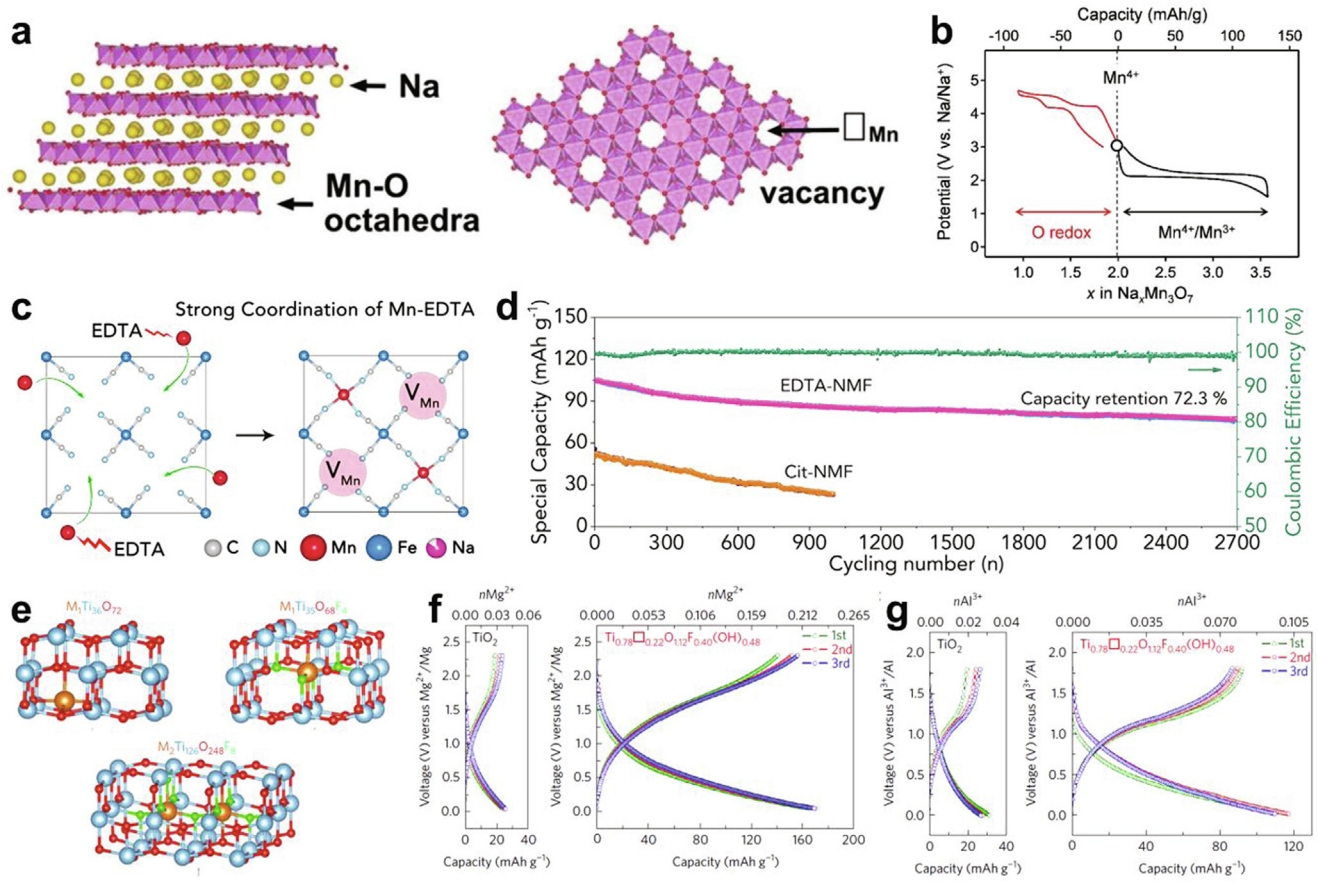

FIGURE 13

(a) The structural illustrations of $Na_{4/7}[\square_{1/7}Mn_{6/7}]O_2$ ($Na_2Mn_3O_7$); Reproduced with permission from Ref. [143]. Copyright 2018, WILEY-VCH Verlag GmbH & Co. KGaA, Weinheim. (b) The charge/discharge profiles of $Na_{4/7-x}[\square_{1/7}Mn_{6/7}]O_2$; Reproduced with permission from Ref. [142]. Copyright 2018, WILEY-VCH Verlag GmbH & Co. KGaA, Weinheim. (c) The formation mechanism of Mn vacancies in EDTA-NMF; (d) the cycling stability of EDTA-NMF and Cit-NMF at 500 mA g^{-1}. Reproduced with permission from Ref. [144]. Copyright 2020, Elsevier Inc. (e) The structural illustrations of the intercalation sites in defect-free $Ti_{36}O_{72}$, single-vacancy $Ti_{35}O_{68}F_4$ and double-vacancy $Ti_{126}O_{248}F_8$ anatase; The electrochemical performance of anatase with and without Ti-vacancy as cathode materials for MIBs (f) and AIBs (g). Reproduced with permission from Ref. [148]. Copyright 2018, Macmillan Publishers Limited, part of Springer Nature.

VO_2, VS_2 and VSe_2 are 1032, 593 to 346 meV, respectively (Fig. 8c–f). The Mg^{2+} diffusion barriers with the trend of oxide > sulfide > selenide was mainly attributed to the different electronegativity (O > S > Se) and ionic radii ($O^{2-} < S^{2-} < Se^{2-}$) of anions, which reduced the interaction between Mg^{2+} and hosts. Besides, higher electronic conductivity and larger interlayer spacing of layered MSe_2 compared to layered MS_2 and MO_2 also facilitate the magnesium diffusion. In addition, the positive effects of Se substitution also have been demonstrated in the conversion-type cathode materials for MIBs. Wang et al. reported the Se-substituted CuS nanosheets as cathode materials for MIBs [86]. Compared to pristine CuS nanosheets, the $CuS_{1-x}Se_x$ ($x = 0.2$) displays enhanced rate performance and cycling stability, which is ascribed to the improved redox reaction kinetics and electrical conductivity.

Except for F and Se substitution, the investigations about other anion substitution in NLIBs cathode materials are still rare. Yu et al. [87] fabricated the $K_{0.6}CoO_{2-x}N_x$ porous nanoframe as cathode material for PIBs. The partial substitution of O atoms by N atoms enhances the electronic conductivity and enlarges the interlayer, facilitating the ion diffusion. Therefore, $K_{0.6}CoO_{2-x}N_x$ with co-enhanced ionic and electronic transport delivers improved capacity and rate performance in PIBs. In addition, Zhang et al. [88] reported that the N substitution and oxygen vacancies can be simultaneously introduced into MnO_2 by a low-temperature NH_3 treatment technology. The N substitution and oxygen vacancies in N-MnO_{2-x} improve the intrinsic electronic conductivity and activity, and thus enhance the electrochemical performance of N-MnO_{2-x} in ZIBs.

The positive effects of anion substitution on electrochemical performance of cathode materials for SIBs and MIBs, especially structural stability and diffusion kinetics, have been demonstrated in some recent works. However, the investigation of anion substitution in cathode materials for other NLIBs is still very rare. On the other hand, the investigation about anion substitution in cathode materials for SIBs and MIBs are focus on F- and Se-substitution. Some other anion such as Cl^-, S^{2-}, N^{3-} could be introduced into cathode materials and may play significant role, which still remain to be investigated in the future research.

Please cite this article in press as: F. Xiong et al., Materials Today, (2021), https://doi.org/10.1016/j.mattod.2020.12.002

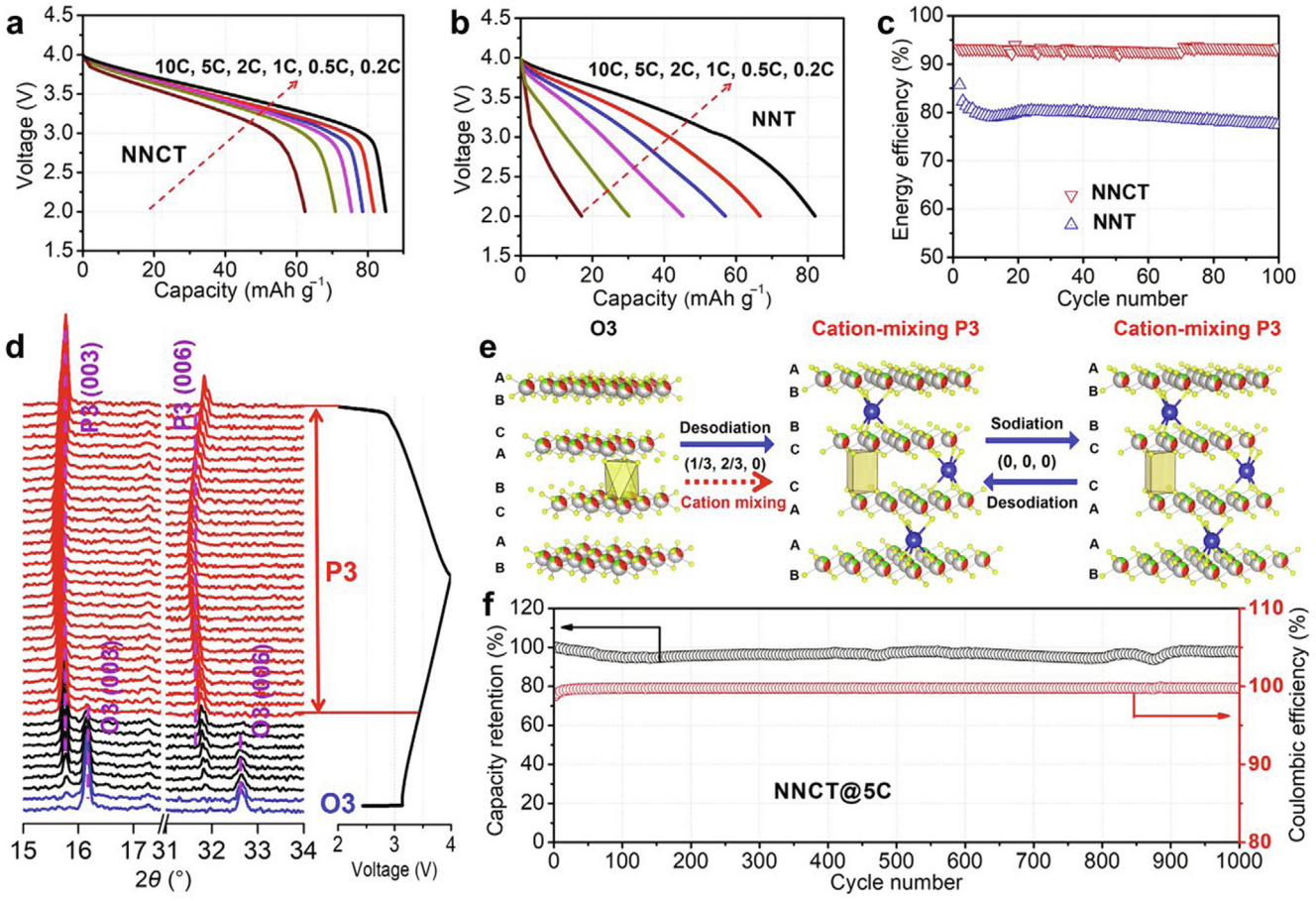

FIGURE 14

The charge/discharge curves at different rates of (a) $Na_{0.8}Ni_{0.3}Co_{0.1}Ti_{0.6}O_2$ (NNCT) with cation disorder and (b) $Na_{0.8}Ni_{0.4}Ti_{0.6}O_2$ (NNT) without cation disorder; (c) cycling stability of NNCT and NNT; (d) *in situ* XRD patterns of NNCT during the first charge/discharge process; (e) schematic illustration for the structural change of NNCT during first charge/discharge process; (f) the long-term cycling performance of NNCT. Reproduced with permission from Ref. [168]. Copyright 2018, Science China Press.

Interstitial impurity

For the cathode materials, the most investigations of interstitial impurity are focus on the layered materials. Generally, the interstitial impurities are located at the interlayer spacing, and it is no doubt that the cations are common impurities in the interlayer owing to the coordination requirements. The introduction of interstitial cation can result in the partial reduction of transition metal in the host and modify the band structure, which usually increases the electronic conductivity. In addition, the "pillaring effect" of interstitial cation would improve the structural stability. Thus, introducing interstitial cation, also be called as cation pre-intercalation, has been considered as an efficient optimization strategy for layered electrode materials. However, introducing interstitial ions will slightly decrease the average discharge potential by reducing the partial transition metal cations. Therefore, it is significant to control the amount of interstitial ions under the premise of ensuring optimization effect. The reported interstitial cation in cathode materials for NLIBs (Table 2) can be classified to alkali metal ion (such as Na^+ and K^+), alkali earth metal ion (such as, Mg^{2+} and Ca^{2+}) and transition metal ion (such as Zn^{2+}, Mn^{2+}, Ni^{2+}, Cu^{2+}, Fe^{3+} and Y^{3+}). In this section, we will summarize the recent progress of cation pre-intercalated cathode materials for NLIBs and discuss the role of various interstitial cation on the improvement of electrochemical performance.

Pre-intercalation of alkali metal ion has been systematically investigated in many cathode materials for LIBs and attempted to be applied in the cathode materials for NLIBs in the recent years [37,138]. The kind of pre-intercalation cation directly impacts the electrochemical performance of hosts. Tang et al. [117] synthesized the alkali-ion pre-intercalated vanadium oxides (A-V_3O_8, A = Li, Na, K) and investigated their magnesium storage performance. With the increase of alkali-ion radius, the interlayer spacings of A-V_3O_8 increase, and the diffusion barriers of pre-intercalation alkali-ion in A-V_3O_8 also increase based on the DFT calculation (Fig. 9a and b), which reflects the improvement of structure stability. However, the layer structure of KV_3O_8 change greatly compared to LiV_3O_8 and NaV_3O_8, which results in low magnesium storage activity. Therefore, the NaV_3O_8 delivers the best magnesium storage performance among three samples (Fig. 9c). In addition, Na-ion pre-intercalated vanadium oxides also delivered improved electrochemical performance in ZIBs. He et al. [118] utilized $Na_{0.33}V_2O_5$ as cathode material for ZIBs, which displays greatly enhanced cycling stability compared to undoped V_2O_5 cathode. After 1000 cycles at 1 A g^{-1}, $Na_{0.33}V_2O_5$ still delivers a capacity of 218.4 mA h g^{-1}, which is over 93%

Please cite this article in press as: F. Xiong et al., Materials Today, (2021), https://doi.org/10.1016/j.mattod.2020.12.002

TABLE 4

Summary of electrochemical performance of amorphous cathode materials for NLIBs.

Materials	Battery system	Highest specific capacity/current density (mAh g^{-1}/mA g^{-1})	Average discharge potential (V)	Rate performance (mAh g^{-1}/mA g^{-1})	Cycling performance (mAh g^{-1}/*n*/mA g^{-1})	Ref.
V_2O_5	SIBs	240/23.6	~2.6 *vs.* Na^+/Na	80/1180	~150/100/23.6	[175]
V_2O_5	SIBs	229.4/40	~2.0 *vs.* Na^+/Na	41.2/5120	54/10000/2560	[176]
V_2O_5/graphene	ZIBs	489/100	~0.75 *vs.* Zn^{2+}/Zn	123/70000	240/3000/30000	[177]
V_2O_5/porous carbon	MIBs	~225/40	~1.3 *vs.* Mg^{2+}/Mg	~100/640	~76/100/320	[178]
V_2O_5/C	AIBs	150/22.1	~0.8 *vs.* Al^{3+}/Al	60/44.2	~75/30/22.1	[179]
MnO_x	ZIBs	250/100	~1.35 *vs.* Zn^{2+}/Zn	64/800	~140/200/100	[180]
MnO_2	ZIBs	328/50	~1.35 *vs.* Zn^{2+}/Zn	164/1200	147/1000/1000	[181]
MnO_2/carbon nantubes	ZIBs	308.5/300	~1.35 *vs.* Zn^{2+}/Zn	69.5/30000	~160/1000/10000	[182]
Mo_3S_{11} cluster	MIBs	115/10	~0.9 *vs.* Mg^{2+}/Mg	–	75/3/10	[183]
$FePO_4$	SIBs	179/10	~2.25 *vs.* Na^+/Na	–	173.6/25/10	[184]
	PIBs	156/4	~2.1 *vs.* K^+/K	–	~130/50/4	
	ZIBs	96/10	~0.75 *vs.* Zn^{2+}/Zn	–	–	
	MIBs	131/5	~0.75 *vs.* Mg^{2+}/Mg	–	–	
$FePO_4 \cdot xH_2O$	SIBs	130/20	~2.25 *vs.* Na^+/Na	31.4/1000	122.4/100/20	[185]
Mesoporous $FePO_4$ nanospheres	SIBs	151/20	~2.34 *vs.* Na^+/Na	44/1000	141/160/20	[186]
2D $FePO_4$	SIBs	168.9/17	~2.25 *vs.* Na^+/Na	77/1700	117.9/1000/170	[187]
$FePO_4$/graphene	SIBs	124/89	~2.25 *vs.* Na^+/Na	41.5/3560	114.3/300/89	[188]
Porous $FePO_4$/CNTs	SIBs	120/10	~2.25 *vs.* Na^+/Na	~50/100	~60/300/50	[189]
$NaFePO_4$	SIBs	115/155	~2.5 vs. Na^+/Na	52/1555	105/800/155	[190]

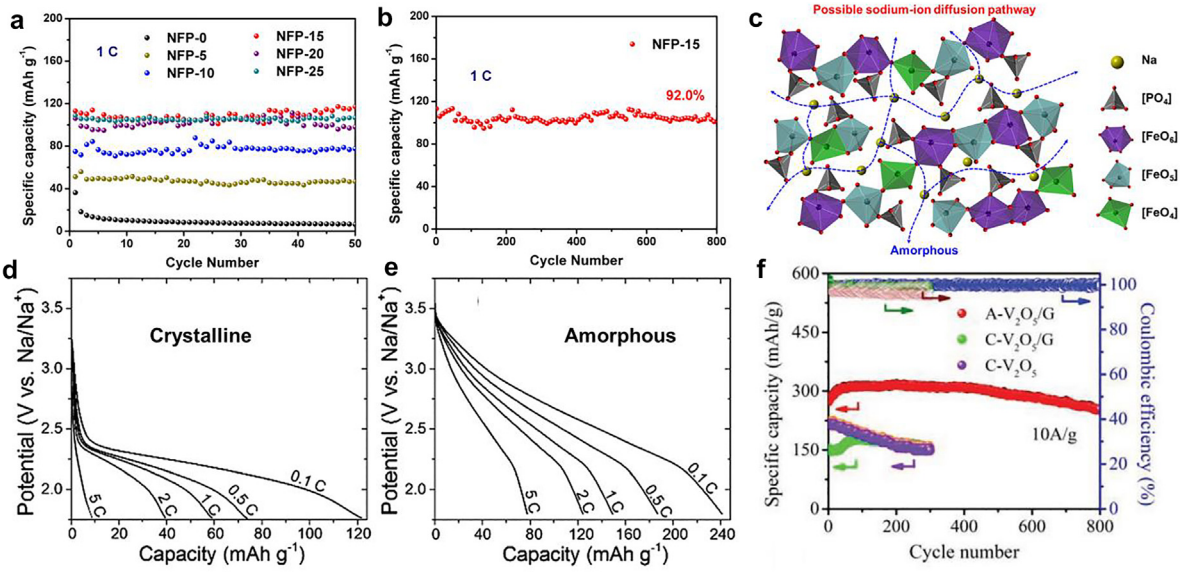

FIGURE 15

(a) The cycling performance of $NaFePO_4$ with different amorphization degree obtained by ball-milling for different time: 0 (NFP-0), 5 (NFP-5), 10 (NFP-10), 15 (NFP-15), 20 (NFP-20) and 25 h (NFP-25); (b) The long-term cycling performance of NFP-15 and (c) the schematic illustrations for possible Na-ion diffusion pathways and atomistic structure for amorphous $NaFePO_4$. Reproduced with permission from Ref. [190]. Copyright 2018, Elsevier Ltd. The discharge curves of (d) crystalline and (e) amorphous V_2O_5 as cathode materials for SIBs; Reproduced with permission from Ref. [175]. Copyright 2014, The Royal Society of Chemistry. (f) Cycling performance of amorphous V_2O_5/graphene composites (A-V_2O_5/G), crystalline V_2O_5/graphene composites (C-V_2O_5/G), and crystalline V_2O_5 (C-V_2O_5). Reproduced with permission from Ref. [177]. Copyright 2020, WILEY-VCH Verlag GmbH & Co. KGaA, Weinheim.

of the highest capacity in the 2nd–1000th cycles (Fig. 9d). Based on the *ex-situ* XRD and TEM technologies, the improved structural stability of $Na_{0.33}V_2O_5$ compared to V_2O_5 during the cycling was demonstrated, which benefit from the "pillar effect" of sodium-ions in interlayer. Similarly, some K-ion pre-intercalated V_2O_5 or MnO_2 also display excellent cycling stability when evaluated as cathode materials for ZIBs [123–125,139]. Besides, the K-ion pre-intercalated bilayered V_2O_5 as cathode materials for PIBs also attract some attention [120–122].

In addition to alkali metal ion, pre-intercalation of alkali earth metal ion also has been applied in the cathode materials for NLIBs, especially multivalent-ion batteries. Compared to

Please cite this article in press as: F. Xiong et al., Materials Today, (2021), https://doi.org/10.1016/j.mattod.2020.12.002

monovalent alkali metal ions, the divalent alkali earth metal ions possess strong polarization, which results in stronger interaction between pre-intercalated ion and host. Thus, the alkali earth metal ion pre-intercalated layered cathode materials may display better structural stability compared to alkali metal ion pre-intercalated one. Pomerantseva and coworkers [140] systemically investigated the bilayered V_2O_5 with the pre-intercalation of various alkali-ions and alkaline-earth-ions. They found that the interlayer spacing of as-prepared bilayered vanadium oxides is positively related to the radii of hydrated ions. Among as-synthesized cation pre-intercalated bilayered V_2O_5, Mg-ion (the maximum hydrated ion) per-intercalated one delivered the largest interlayer spacing (13.40 Å). Xu et al. [126] fabricated the Mg-ion pre-intercalated bilayered V_2O_5 ($Mg_{0.3}V_2O_5{\cdot}1.1H_2O$) (Fig. 10a) and employed it as cathode materials for MIBs. The pre-intercalation Mg-ions improve the electronic conductivity and stabilize the layer structure (Fig. 10b). The interlayered water molecules enlarge the interlayer spacing and hold "charge shielding effect", facilitating the diffusion of magnesium-ion. Benefiting from the synergistic effects of interlayered water molecules and pre-intercalated Mg-ions, the $Mg_{0.3}V_2O_5{\cdot}1.1H_2O$ displayed improved cycling stability and rate performance (Fig. 10c and d). Meanwhile, $Mg_{0.3}V_2O_5{\cdot}1.1H_2O$ exhibited ultra-long cycling life that a capacity of about 90 mAh g^{-1} was achieved after 10,000 cycles at 2 A g^{-1}, corresponding to 80% of the maximum capacity (Fig. 10e). Moreover, $Mg_xV_2O_5{\cdot}nH_2O$ also exhibited excellent cycling stability when evaluated as cathode materials for both ZIBs [127] and calcium-ion batteries (CIBs) [128], further confirming the availability of Mg-ion pre-intercalation in enhancing cycling stability of $V_2O_5{\cdot}nH_2O$. Except for Mg-ion, Ca-ion, another alkali earth metal ion, also has been employed in the interlayer regulation of cathode materials for NLIBs [129–131]. For example, Tao et al. [131] investigated the electrochemical performance of Ca-ion pre-intercalated manganese oxide ($Ca_{0.28}MnO_2{\cdot}0.5H_2O$) in ZIBs, and confirmed the positive effect of Ca-ion in interlayer on rate capability and cycling performance. In addition, Ca-ion pre-intercalated $V_2O_5{\cdot}nH_2O$ ($Ca_{0.25}V_2O_5{\cdot}nH_2O$) as cathode materials for ZIBs also delivered excellent cycling stability [129].

Due to the large interlayer spacing, many transition metal ions also can be pre-intercalated into $V_2O_5{\cdot}nH_2O$ [132–137,141]. For example, Wei et al. [132] utilized the layered vanadium oxide xerogel with the pre-intercalation of iron-ion as SIBs cathode materials. The iron pre-intercalated vanadium oxide possesses stabilized interlamellar spacing and inhibited lattice breathing during the sodium-ion intercalation/deintercalation process (Fig. 11a). Different from the rapid decrease of d_{001} for vanadium oxide xerogel in the first three cycles, the d_{001} of iron pre-intercalated cathode stabilizes after first charge/discharge process (Fig. 11b). Moreover, the stabilized d_{001} of iron pre-intercalated vanadium oxide after first several cycles is larger than that of original vanadium oxide. As a result, the enhanced cycling stability and rate performance of iron pre-intercalated cathode was obtained. Recently, $V_2O_5{\cdot}nH_2O$ with the pre-intercalation of various transition metal ion, such as Zn^{2+} [136], Cu^{2+} [141], Mn^{2+} [134], Co^{2+} [134], and Ni^{2+} [133,134], has been investigated as cathode materials for zinc-ion storage. Nazar et al. [136] reported the electrochemical performance of $Zn_{0.25}V_2O_5{\cdot}nH_2O$ as cathode material for ZIBs (Fig. 11c and d). The pre-intercalated Zn-ions stabilize the layered structure thus ensure the cycling stability. Consequently, the capacity retention of $Zn_{0.25}V_2O_5{\cdot}nH_2O$ cathode is over 80% after cycling at 2400 mA g^{-1} for 1000 cycles. Cao and co-workers investigated the zinc storage performance of Mn^{2+}, Co^{2+} and Ni^{2+} pre-intercalated $V_2O_5{\cdot}nH_2O$ [134]. Compared to $V_2O_5{\cdot}nH_2O$, three transition metal ion pre-intercalated samples delivers the improved capacities, rate performances and cycling stabilities and Mn^{2+} pre-intercalated $V_2O_5{\cdot}nH_2O$ exhibits the best zinc storage performance. A high reversible capacity of 415 mA h g^{-1} was achieved at 50 mA g^{-1} and capacity remained at 260 mA h g^{-1} when current density up to 4 A g^{-1}. Moreover, after cycling at 4 A g^{-1} for 2000 cycles, the capacity retention is as high as 92%. The enhanced performances of Mn^{2+} pre-intercalated $V_2O_5{\cdot}nH_2O$ originate from the enlarged interlayer spacing, the "pillar effect" of Mn^{2+}, and improved reaction kinetics. In addition, the Mn-ion pre-intercalated $V_2O_5{\cdot}nH_2O$ exhibited outstanding magnesium storage performance [135].

In summary, introducing interstitial cation can improve the electrochemical performance of many cathode materials by the pillar effect and expanding diffusion pathway. For hydrated layered transition metal oxides, the cation pre-intercalation can inhibit the lattice breathing during the cycling. Moreover, the species and amount of pre-intercalated cation, as well as the pristine structure of host greatly impact the intrinsic coordination state of pre-intercalated electrode materials, modifying the specifically insufficient factor and improving the electrochemical performance. However, the most investigations about interstitial cation in cathode materials for NLIBs are focus on vanadium oxides, only few works on other oxides, such as layered molybdenum oxides and tunnel-type manganese oxides. Extending the cation pre-intercalation to other cathode materials still need more efforts.

Vacancy defect

Vacancy defect is another kind of point defect, which is refers to atoms or ions missing from the lattice sites. The formation of vacancy would impact the local structure and charge distribution, playing significant role in the modification of electrochemical performance of cathode materials. According to the species of missing ion at corresponding lattice sites, the vacancy defect can be classified to anion vacancy and cation vacancy. Here, we focus on the recent investigations about vacancy defects in cathode materials for NLIBs (Table 3).

Some investigations demonstrated that the oxygen vacancies in layered transition metal oxides can enhance the electronic conductivity by tunning the band gap and facilitate the sodium-ion diffusion [158,159,161–163]. Different to the lithium counterpart, the sodium/transition metal disorder was minimized due to the large gap in ionic radii between sodium-ion and transition metal ion (such as Ni^{2+}). Therefore, the oxygen vacancies in layered sodium transition metal oxides play positive role on improving electrochemical performance. For example, the $NaMnO_{2-y-\delta}(OH)_{2y}$ with oxygen vacancies reported by Xia et al. displays improved specific capacity and rate performance [159]. The DFT calculation delivered that the band gap of monoclinic $NaMnO_2$ decreases from 1.25 to 0.24 eV after

Please cite this article in press as: F. Xiong et al., Materials Today, (2021), https://doi.org/10.1016/j.mattod.2020.12.002

introducing 4 at% O vacancies, indicating that the introduction of oxygen vacancies can improve the electronic conductivity. Xu et al. reported that the sodium storage performance of MoO_3 can be improved by introducing oxygen vacancies [163]. Compared to pristine MoO_3, MoO_{3-x} with oxygen vacancies exhibits improved electronic conductivity and sodium-ion diffusivity, and thus delivers better rate performance.

Besides, introducing oxygen vacancy has also been employed to promote the electrochemical performance of cathode materials for multivalent-ion batteries [52,149,150,156,157,164]. For instance, Li et al. presented oxygen vacancy-rich VO_2 as cathode materials for ZIBs [150]. The DFT calculations demonstrate that introducing oxygen vacancies into VO_2 narrowed the band gap and reduced the Zn-ion diffusion energy barrier (Fig. 12a and b). Therefore, oxygen vacancy-rich VO_2 ($VO_{1.75}$) exhibits enhanced reaction kinetics and Zn-ion storage performance (Fig. 12c). Soon afterward, Luo et al. [151] combined the oxygen vacancy introduction with heterojunction engineering to further improve the electrochemical performance of VO_2 in ZIBs. Consequently, even at the high current density of 20 A g^{-1}, a capacity of 116 mAh g^{-1} was still remained. Moreover, the capacity retention of 88.6% was obtained after 5000 cycles at 10 A g^{-1}. In addition, oxygen-deficient V_6O_{13} also delivers better electrochemical performance as cathode materials for ZIBs compared to pristine one [152,153]. Similarly, oxygen vacancies also plays positive role on the electrochemical performance of Mn-based cathode materials for ZIBs [52,156,164]. Specially, various strategies have been employed to creating oxygen vacancies in MnO_2 cathode for ZIBs, including chemical reduction [155,165,166], chemical pre-intercalation [156], and cation/anion substitution [88,160]. The DFT calculation results demonstrate that the oxygen vacancies in σ-MnO_2 enhance the reversibility of Zn^{2+} adsorption/desorption process (Fig. 12d), which account for the better electrochemical performance of oxygen-deficient MnO_2 obtained by chemical reduction compared to less defective one [155]. Moreover, the oxygen vacancies may open the [MnO_6] octahedral walls in α-MnO_2, which facilitates ion diffusion in *ab*-plane and enhances the reaction kinetics (Fig. 12e) [52,156]. In addition, introducing oxygen vacancy has been identified as a way to improve the Mg-ion and Al-ion storage performance of metal oxides. For instance, the vacancy-rich TiO_{2-x} nanoflakes [149] and WO_{3-x} nanorods [157] exhibit the increased capacity when evaluated as cathode materials for MIBs and aluminum-ion batteries (AIBs), respectively.

Except for anion vacancies, some researchers also pay attention to the cation vacancies in cathode materials [81,142–144,148,167]. For instance, introducing transition metal vacancies is a possible method to activate anionic redox of layered oxides. The presence of transition metal vacancies will creates the Na-O-vacancy and vacancy-O-vacancy configurations with nonbonding oxygen 2p orbitals, thus facilitating the oxygen redox reaction. Ma et al. demonstrated the oxygen activity of P2-type $Na_{0.78}Ni_{0.23}Mn_{0.69}O_2$ with vacancies in transition metal layer [167]. Although the attained reversible oxygen-redox capacity only 40 mAh g^{-1} due to the small quantity of transition metal vacancies (7%), this work confirms the promise of exploiting SIBs cathode materials with oxygen redox by fabricating transition metal vacancies. Yamada and coworkers reported that the $Na_{4/7-x}[\square_{1/7}Mn_{6/7}]O_2$ ($Na_2Mn_3O_7$) with inherent Mn vacancies (Fig. 13a) displays highly reversible oxygen redox activity (75 mAh g^{-1}) at over 4.0 V (*vs.* Na^+/Na) (Fig. 13b) [142]. In contrast, the vacancy-free layered counterpart ($Na_{2/3}MnO_2$) exhibits negligible capacity over 4.0 V (*vs.* Na^+/Na). The oxygen redox activity of $Na_{4/7-x}[\square_{1/7}Mn_{6/7}]O_2$ originates from the nonbonding 2p orbitals of oxygens around Mn vacancies. Moreover, Li et al. reported that $Na_{4/7}[\square_{1/7}Mn_{6/7}]O_2$ is zero-strain during the Na extraction/insertion, resulting in superior structural flexibility and stability [143]. In addition, the cation-deficient manganese oxides also display superior electrochemical performance in ZIBs [145,146]. Different from the difficult Zn-ion diffusion in stoichiometric $ZnMn_2O_4$ spinels, the Mn-defected $ZnMn_2O_4$ exhibits higher mobility of Zn-ion due to that the Mn vacancies facilitate the Zn-ion diffusion [146].

Most recently, Shang et al. found that introducing Mn vacancies into Mn–Fe Prussian blue analogs (PBAs) can inhibit the Jahn-Teller distortion and realize ultrastable cycling performance [144]. They fabricated the Mn-Fe PBAs with a large amount of Mn vacancies on the surface (EDTA-NMF) by using ethylene diaminetetraacetic acid disodium (Na_2EDTA) to remove the Mn atoms from the crystal lattice (Fig. 13c). Compared to Mn-Fe PBAs without Mn vacancies (Cit-NMF), EDTA-NMF delivers highly improved cycling stability with capacity retention of 72.3% after 2700 cycles (Fig. 13d). The *in-situ* XRD and DFT calculation results demonstrate that structure deformation of EDTA-NMF upon the Na^+ insertion/extraction was efficiently suppressed owing to the presence of Mn vacancies, which is responsible for the enhanced cycling stability.

Moreover, cation vacancies can be act as intercalation sites in some case, which makes the higher capacity achievable. Koketsu et al. [148] introduced a large amount of Ti vacancies into TiO_2 by F doping and investigated the magnesium-ion and aluminum-ion storage behaviors in as-prepared cation-deficient TiO_2. The DFT calculations imply that the intercalation energies for Li, Mg, and Al decrease in the F-doped anatase systems with Ti vacancies compared to those in anatase TiO_2 (Fig. 13e). Moreover, all three ions prefer to intercalate into titanium vacancies in Ti-vacancy-rich TiO_2. Consequently, cation-deficient TiO_2 displays greatly improved magnesium and aluminum storage capacity, i.e., from 25 and 30 mA h g^{-1} to 165 and 120 mA h g^{-1}, respectively (Fig. 13f and g). In this cation-deficient TiO_2, the F substitution and cation vacancies were co-existed, but the effect of F substitution on the electrochemical performance was not well investigated. The synergetic effects of anion substitution and cation vacancies may also play important role in the enhancement of electrochemical performance. [81]

Introducing suitable anion vacancy defects can improve the electronic conductivity and ionic diffusivity of cathode materials, thus plays positive role in rate performance. Cation vacancies in cathode materials also enhance the diffusion kinetics and may act as intercalation sites. Although the above advantages of vacancy defects have been demonstrated in some cases, their mechanism in many cathode materials are still unclear due to the limited investigation, which need further research in the future. In addition, how to rationally create the cation vacancies in cathode materials is still a challenge.

Please cite this article in press as: F. Xiong et al., Materials Today, (2021), https://doi.org/10.1016/j.mattod.2020.12.002

Cation disorder

Cation disorder was usually affected by substitutional impurity, but it is a kind of crystal defect different from substitutional impurity. Cation disorder, also known as cation mixing, is referred to the disordering of cation arrangement. According to the kinds of involved cations, cation disorder can be classified to A/TM disorder and TM/TM disorder (A = alkali metal or alkali earth metal, TM = transition metal). Generally, A/TM disorder was harmful for the electrochemical performance of cathode materials. For example, the TM-ions in Li/Na slab will hinder the Li/Na ion diffusivity, resulting in the capacity decay and the structural degradation. Interestingly, some recent works demonstrated that the A/TM disorder can play a positive role in the cathode materials of SIBs. In addition, TM/TM disorder also plays important role on modifying electrochemical performance of layered cathode materials for SIBs.

The A/TM disorder in some special case displayed positive effects on electrochemical performance and some cation-disordered rocksalt oxides delivered attractive high capacity. For instance, Guo et al. reported that the undesired Na/TM disorder can stabilize the P3-type structure and result in enhanced rate capability and cycling stability (Fig. 14a–c) [168]. Based on the *in-situ* XRD (Fig. 14d) and *ex-situ* scanning transmission electron microscopy (STEM) experiments, they found that the O3-type $Na_{0.8}Ni_{0.3}Co_{0.1}Ti_{0.6}O_2$ transforms to P3-type during the first charge process as most and O3-type layered oxide cathode materials for SIBs, but maintained the P3-stacking in the subsequent cycles due to the Na/TM disorder occurred after first charge process (Fig. 14e). Moreover, the obtained P3-type $Na_{0.8}Ni_{0.3}Co_{0.1}Ti_{0.6}O_2$ delivers the very low lattice strain. Consequently, $Na_{0.8}Ni_{0.3}Co_{0.1}Ti_{0.6}O_2$ exhibits improved capacity retention of 98% after 1000 cycles (Fig. 14f). Sato et al. employed the Na-excess cation-disordered rocksalts ($Na_{1.3}Nb_{0.3}Mn_{0.4}O_2$) as cathode materials for SIBs, which displayed a high reversible specific capacity about 200 mA h g^{-1} [169]. The reasons for the unexpected sodium storage activity in Na-excess cation-disordered rocksalts may be similar with that of lithium storage activity in Li-excess cation-disordered rocksalts. Ceder et al. confirmed that the percolation of certain active diffusion channels is responsible for unexpected electrochemical behavior of Li-excess cation-disordered rocksalts [170].

The arrangement of transition metal in layered cathode materials for SIBs will affect the charge order and Na/V_{Na} order. Wang et al. reported that the Cr^{3+}/Ti^{4+} disorder in P2-$Na_{0.6}[Cr_{0.6}Ti_{0.4}]O_2$ electrode broken the charge ordering and resulted in Na/V_{Na} disorder [171]. The Na/V_{Na} disorder can accelerate sodium-ion diffusion and eliminate the complex multi-step phase transition during the charge/discharge process. Therefore, the P2-$Na_{0.6}[Cr_{0.6}Ti_{0.4}]O_2$ delivered excellent rate capability and cycling stability. The transition metal ordering in binary layered $Na_x[M1, M2]O_2$ is mainly depended on the ionic radii of M1 and M2. The small difference (below 15%) in the ionic radii of M1 and M2 tends to result in TM/TM disordering. In addition, the charge ordering is associated with the Fermi level (redox potential) of M1 and M2. The large difference in Fermi level of M1 and M2 tends to result in charge disordering. Furthermore, the charge order and Na/V_{Na} order are coupled with each other. Therefore, TM/TM disordered layered cathode materials can be obtained by choosing transition metal ions. Many layered SIBs cathode materials with two or more transition metal, such as $Na_xCo_{0.1}Mn_{0.9}O_2$ [61], $Na_{0.67}Co_{0.9}Ti_{0.1}O_2$ [172], $Na_{2/3}Ni_{1/3}Mn_{1/3}Ti_{1/3}O_2$ [50], and so forth, displayed enhanced rate performance and cycling stability due to the suppression of Na/V_{Na} ordering, in which TM/TM disorder may also plays important role.

In conclusion, the rationally utilizing A/TM disorder in layered oxide cathode materials can improve the electrochemical performance. Introducing TM/TM disorder may be an efficient way to enhance the rate capability and cycling performance of layered cathode materials for SIBs by suppressing the Na/V_{Na} ordering. However, the investigations of cation disorder in cathode materials for NLIBs are still relatively rare. The accurate control of cation disorder degree and rational utilization of the A/TM disorder still fill of challenge.

Amorphization

The structural destruction (amorphization) of electrode materials during the charge/discharge process has been considered as one of the most important reasons for capacity fading [173,174]. The ion storage sites provided by ordered atomic arrangement could be invalid following the collapse of ordered structure. Interestingly, some special amorphous materials can provide a disordered framework for ion storage and even displays better electrochemical performance than their crystalline categories (Table 4). In this section, we review these special amorphous electrode materials and discuss the origin of these unexpected properties.

Maricite $NaFePO_4$, the thermodynamically stable phase, has been demonstrated as a cathode material with low electrochemical activity due to its high activation barriers for Na diffusion [27]. Excitingly, Kim et al. [191] reported that the amorphous $FePO_4$ obtained from maricite $NaFePO_4$ in the first charge process displays unexpectedly high sodium-ion storage activity during the subsequent cycling. The reversible capacity of 142 mAh g^{-1} was obtained at C/20 (1 C = 155 mA g^{-1}) and remained after 200 cycles without obvious fading. The unexpected electrochemical activity is attributed to the possible sodium diffusion pathway with low activation barriers in the amorphous $FePO_4$. Kapaev et al. [192] demonstrated that the maricite $NaFePO_4$ after partial amorphization by ball milling treatment can also display high electrochemical activity. Recently, the atom-scale structure and the enhancement mechanism of amorphous $NaFePO_4$ also have been investigated. Xiong et al. [190] prepared the $NaFePO_4$ composites with different disorder degrees by adjusting the ball-milling parameter, and verified that the sodium storage capacity has positive dependence on the disorder degree (Fig. 15a). The optimized $NaFePO_4$ composite displays enhanced capacity (115 mAh g^{-1}) and the high capacity retention of 91.3% after 800 cycles (Fig. 15b). Moreover, the atomistic origin of the disorder-enhanced sodium storage performance was clarified by XANES and Raman spectroscopy. They found that edge-sharing FeO_6 octahedra transform to various FeO_n polyhedra upon amorphization, which has been considered as a key for enhancing sodium storage performance (Fig. 15c). Except for the ball milling, some other methods have also been attempted to attain amorphous

Please cite this article in press as: F. Xiong et al., Materials Today, (2021), https://doi.org/10.1016/j.mattod.2020.12.002

$NaFePO_4$. The conventional melt-quenching method is unsuccessful as $NaFePO_4$ is on outside of the glass formation region for $NaO_{0.5}$-FeO-$PO_{2.5}$ system [193]. But the $Na_{1.1}Fe_{0.9}P_{1.1}O_{4.2}$ and $Na_{1.2}Fe_{0.8}P_{1.2}O_{4.4}$ glasses can be obtained via melt-quenching method and exhibit high sodium storage capacity.

Meanwhile, amorphous $FePO_4$ is also a promising cathode material for NLIBs [184,186,189]. Compared with crystalline forms, amorphous $FePO_4$ delivers higher capacity as the amorphous structure provides more intercalation sites for sodium-ion. On the other hand, amorphization could break the diffusion barriers and offer some possible ion transport pathways, facilitating ion diffusion. Mathew et al. [184] evaluated the electrochemical performance of amorphous $FePO_4$ as cathode materials for various metal-ion batteries, including LIBs, SIBs, PIBs, MIBs, ZIBs and AIBs. The amorphous $FePO_4$ displays high capacity in all those batteries.

The orthorhombic V_2O_5 is an excellent cathode material with high capacity for LIBs. However, as cathode material for SIBs, orthorhombic V_2O_5 displays low average discharge potential and capacity, which results from that the interlayer spacing of orthorhombic V_2O_5 is unsuitable for reversible sodium-ion intercalation/deintercalation [194]. Uchaker et al. [175] compared the sodium storage performance of the orthorhombic and amorphous V_2O_5. The amorphous V_2O_5 displays better sodium storage performance with higher average discharge potential and capacity as well as better cycling stability (Fig. 15d and e). The superior sodium storage performance of amorphous V_2O_5 is attributed to the more open channels, which is benefit for the sodium-ion diffusion. In addition, the amorphous surface also facilitates the penetration of sodium-ion into structure. Therefore, the lower overpotential was obtained in amorphous V_2O_5, which results in higher discharge potential. Moreover, the greater Gibbs free energy of formation of amorphous V_2O_5 also enhances the discharge potential [24]. Recently, amorphous V_2O_5 also exhibits attractive electrochemical performance in multivalent-ion batteries. The amorphous V_2O_5/graphene composites reported by Wang et al. [177] displayed the improved capacity and cycling stability in ZIBs, compared to crystalline V_2O_5/graphene composites (Fig. 15f). Besides, amorphous V_2O_5 also delivers considerable electrochemical activity in MIBs and AIBs [178,179]. But whether amorphous V_2O_5 better than crystalline one for MIBs and AIBs still needs further study.

Recently, amorphous manganese oxides also attract some attention in the researches on cathode materials for ZIBs [180–182]. For example, Wu et al. [180] presented the mesoporous amorphous manganese oxide (UCT-1–250) as cathode material for ZIBs, which displays improved capacity compared to other tunnel crystalline phases. The better electrochemical performance was attributed to the fast in situ formation of $ZnMn_2O_4$ resulted from the existence of mesopores and oxygen vacancies. Srinivasan et al. [181] reported the electrochemical behaviors of amorphous manganese dioxide in ZIBs. The abundant oxygen vacancies and void spaces in amorphous manganese dioxide result in the high surface reactivity and the enhanced capacitive storage behavior, which has significant effect on the excellent rate capability and cycling stability. Furthermore, Bi et al. [182] fabricated the amorphous MnO_2/carbon nanotubes composite and realized the further improved electrochemical performance.

Amorphization can improve the electrochemical performance but only effective for some certain cathode materials. The amorphization may break the confinement of ordered crystal structure and create some new ion diffusion channels, thus changes the electrochemical activity. In addition, some recent investigations demonstrated that constructing crystal/amorphous composites, i.e., ordering/disordering engineering is an effective strategy to modify the electrochemical performance [195–197]. Although some possible improvement mechanisms have been proposed, the exact role of amorphization in cathode materials is still ambiguous as the atomic-scale structure of amorphous phase is difficult to be determined.

Summary and outlook

Crystal defect modulation is a significant strategy for developing high-performance electrode materials for various NLIBs. This review endeavors to emphasize the positive effects of crystal defects on the electrochemical performances of cathode materials for NLIBs including SIBs, PIBs, MIBs, CIBs, ZIBs and AIBs, and focus on the substitutional impurity, interstitial impurity, vacancy defect, cation disorder and amorphization. The intentionally introduced defects are able to change the electronic conductivity, ionic diffusivity, structural stability, ion storage site, reaction redox couple and so forth. Therefore, most electrochemical performances including capacity, operating potential, cycling stability and rate performance can be modified by crystal defect modulation.

Cation substitution plays important role in modifying the electronic conductivity, ionic diffusivity, structural stability and reaction redox couple of cathode materials. The effects and work mechanism of substitutional cation in cathode materials for SIBs is studied systematically, and many obtained rules and theories can be employed in the cathode materials for other NLIBs, especially PIBs. For multivalent-ion batteries, the development of cathode materials is restrained by the strong interaction between multivalent-ion and host and anion substitution is an effective way to solve this problem. Cation pre-intercalation is not only widely applied in the cathode materials for SIBs, MIBs and ZIBs, but also confirmed as an efficient approach to exploit the cathode materials for PIBs and CIBs. Oxygen vacancy defects in cathode materials can increase the electronic conductivity and ionic diffusivity, meanwhile cation vacancies may be acted as ion storage sites. Cation disorder and amorphization are harmful for the electrochemical performance of many cathode materials for NLIBs, but they also play positive effects in some cases. Recent investigations display that many reported cation-disordered or amorphous cathode materials exhibit excellent electrochemical performance and some even better than that of well-ordered one. Besides, the electrochemical performance of cathode materials for NLIBs may also be affected by many crystal defects which have not been discussed above, such as twin boundary, stacking faults and others. For example, the significant effect of defective tunnel intergrowth on sodium storage performance has been demonstrated in MnO_2 [198]. However, relevant works are still rare, and some future works may focus on these interesting defects. Different crystal defects play different roles, and we hope that this review can provide guidance for choosing suitable

Please cite this article in press as: F. Xiong et al., Materials Today, (2021), https://doi.org/10.1016/j.mattod.2020.12.002

crystal defect modulation to solve the existed issue of cathode materials for NLIBs.

Although many progresses had been demonstrated, some issues and challenges still existed, such as quantificationally controllable strategy to create uniform and homogeneous defects, comprehensive structure-performance relationship for various crystal defects and so forth. Moreover, harmful defects and how to minimize the negative effects of defects should be taken into account before introducing a defect. The impurity defects have been investigated widely and systematically, but the research of vacancy defect (especially cation vacancy), cation disorder and amorphization in cathode materials for NLIBs are still in the condition of initial period. The enhancement mechanism and the systematically structure-performance relationship of amorphous cathode materials have a long way to go before fully established. Moreover, the combination of multiple defects may realize the further improvement of electrochemical performance of NLIBs cathode materials, but the investigations on the synergetic effects of multiple defects are still rare. By crystal defect modulation, many cathode materials for NLIBs display excellent electrochemical performance (Tables 1–4). Among these, some cathode materials display the attractive energy density of over 400 Wh kg^{-1} for nonaqueous systems or 250 Wh kg^{-1} for aqueous systems and the cycling life of over 1000 cycles, demonstrating the potential for practical application. However, many factors should be considered, such as the electrochemical performance at high mass loading, the cost, the match of cathode materials with anode materials, and so forth. Continuous works are still needed for the further development of crystal defect modulation on cathode materials for NLIBs. We believe that crystal defect modulation will not only play important role in developing high-performance cathode materials, but also offer significant insights for exploiting novel cathode materials for NLIBs.

Declaration of Competing Interest

The authors declare that they have no known competing financial interests or personal relationships that could have appeared to influence the work reported in this paper.

Acknowledgements

This work was supported by the National Key Research and Development Program of China (2020YFA0715000, 2016YFA0202603), the National Natural Science Foundation of China (51832004, 51521001, 51872218, 51972259), Foshan Xianhu Laboratory of the Advanced Energy Science and Technology Guangdong Laboratory (XHT2020-003).

References

[1] D. Larcher, J.M. Tarascon, Nat. Chem. 7 (2015) 19–29.
[2] S. Chu, A. Majumdar, Nature 488 (2012) 294–303.
[3] H. Pan et al., Energy Environ. Sci. 6 (2013) 2338–2360.
[4] M. Chen et al., Adv. Energy Mater. 9 (2019) 1803609.
[5] T. Jin et al., Chem. Soc. Rev. 49 (2020) 2342–2377.
[6] F. Wang et al., Adv. Mater. 32 (2020) 2000287.
[7] S. Hu et al., Electrochem. Energy Rev. 2 (2019) 277–311.
[8] T. Li et al., Electrochem. Energy Rev. 3 (2019) 43–80.
[9] B. Xiao, X. Sun, Adv. Energy Mater. 8 (2018) 1802057.
[10] Y. Sun et al., Adv. Energy Mater. 9 (2018) 1800212.
[11] M. Mao et al., Chem. Soc. Rev. 47 (2018) 8804–8841.
[12] T. Hosaka et al., Chem. Rev. 120 (2020) 6358–6466.
[13] M. Song et al., Adv. Funct. Mater. 28 (2018) 1802564.
[14] F. Wu et al., Adv. Mater. 31 (2019) 1806510.
[15] J. Muldoon et al., Chem. Rev. 114 (2014) 11683–11720.
[16] H. Tang et al., Electrochem. Energy Rev. 1 (2018) 169–199.
[17] N. Yabuuchi et al., Chem. Rev. 114 (2014) 11636–11682.
[18] P.-F. Wang et al., Adv. Energy Mater. 8 (2018) 1701912.
[19] H. Li et al., Adv. Funct. Mater. 30 (2020) 2000473.
[20] Q. Wei et al., Adv. Mater. 29 (2017) 1602300.
[21] X. Xu et al., Adv. Funct. Mater. 30 (2020) 1802564.
[22] F. Wang et al., Energy Environ. Sci. 9 (2016) 3570–3611.
[23] Y. Zhang et al., Adv. Mater. 32 (2020) 1905923.
[24] E. Uchaker, G. Cao, Chem. Asian J. 10 (2015) 1608–1617.
[25] F. Yu et al., Energy Storage Mater. 22 (2019) 235–255.
[26] S. Tan et al., Mater. Horiz. 7 (2020) 1971–1995.
[27] P.P. Prosini et al., Solid State Ionics 263 (2014) 1–8.
[28] S. Komaba et al., Electrochem. Commun. 12 (2010) 355–358.
[29] A. Van der Ven et al., Acc. Chem. Res. 46 (2012) 1216–1225.
[30] J. Meng et al., Joule 1 (2017) 522–547.
[31] K. Toyoura et al., Phys. Rev. B 78 (2008) 214303.
[32] J.B. Goodenough, Y. Kim, Chem. Mater. 22 (2010) 587–603.
[33] B.C. Melot, J.M. Tarascon, Acc. Chem. Res. 46 (2013) 1226–1238.
[34] J. Gao et al., Chin. Phy. B 25 (2016) 018210.
[35] H. Kim et al., Chem. Mater. 28 (2016) 7241–7249.
[36] Y. Chen et al., J. Power Sources 378 (2018) 423–432.
[37] X. Yao et al., ACS Energy Lett. 4 (2019) 771–778.
[38] Q. Zheng et al., J. Mater. Chem. A 6 (2018) 4209–4218.
[39] P.-F. Wang et al., Angew. Chem. Int. Ed. 55 (2016) 7445–7449.
[40] G. Singh et al., Chem. Mater. 28 (2016) 5087–5094.
[41] R.J. Clément et al., Energy Environ. Sci. 9 (2016) 3240–3251.
[42] H. Li et al., J. Mater. Chem. A 3 (2015) 9578–9586.
[43] J. Weng et al., Chem. Eng. J. 392 (2020) 123649.
[44] R. Dang et al., J. Power Sources 464 (2020) 228190.
[45] W. Kong et al., J. Mater. Chem. A 7 (2019) 9099–9109.
[46] P.-F. Wang et al., Nano Energy 69 (2020) 104474.
[47] I. Hasa et al., J. Mater. Chem. A 5 (2017) 4467–4477.
[48] M.J. Aragón et al., Electrochim. Acta 180 (2015) 824–830.
[49] S.-J. Lim et al., J. Mater. Chem. A 2 (2014) 19623–19632.
[50] P.F. Wang, et al., Sci. Adv. 4 (2018) eaar6018.
[51] H. Yi et al., Nano Energy 47 (2018) 340–352.
[52] S. Lian et al., Nano Energy 62 (2019) 79–84.
[53] X. Zhang et al., Chem. Commun. 56 (2020) 6293–6296.
[54] A. Criado et al., J. Electroanal. Chem. 856 (2020) 113694.
[55] W. Zhou et al., Nano Lett. 16 (2016) 7836–7841.
[56] C.-L. Liu et al., Chem. Eng. J. 378 (2019) 122167.
[57] Y. Zhang et al., ACS Cent. Sci. 6 (2020) 232–240.
[58] L. Zhou et al., Nano Energy 54 (2018) 360–366.
[59] L. Mu et al., Adv. Mater. 27 (2015) 6928–6933.
[60] Z.-Y. Li et al., ACS Appl. Mater. Interfaces 8 (2016) 15439–15448.
[61] N. Bucher et al., Chem. Mater. 28 (2016) 2041–2051.
[62] J.Y. Hwang et al., Nat. Commun. 6 (2015) 6865.
[63] F. Kataoka et al., ACS Appl. Energy Mater. 3 (2020) 4720–4726.
[64] K. Kaliyappan et al., Adv. Funct. Mater. 28 (2018) 1801898.
[65] Y. Tao et al., Electrochim. Acta 331 (2020) 135296.
[66] P. Bai et al., ACS Appl. Mater. Interfaces 12 (2020) 10490–10495.
[67] W. Kang et al., ACS Appl. Mater. Interfaces 8 (2016) 31661–31668.
[68] Y. Li et al., Adv. Sci. 2 (2015) 1500031.
[69] T.R. Chen et al., ACS Appl. Mater. Interfaces 10 (2018) 10147–10156.
[70] L. Yang et al., Chem. Eng. J. 404 (2021) 126578.
[71] N. Liu et al., ACS Appl. Mater. Interfaces 12 (2020) 28199–28205.
[72] X. Wu et al., J. Power Sources 281 (2015) 18–26.
[73] Z.-Y. Li et al., Electrochim. Acta 223 (2017) 92–99.
[74] W. Liu et al., J. Mater. Chem. A 5 (2017) 10928–10935.
[75] X. Li et al., J. Mater. Chem. A 6 (2018) 1390–1396.
[76] Y. Zhang et al., J. Mater. Chem. A 6 (2018) 4525–4534.
[77] K. Liu et al., Adv. Energy Mater. 10 (2020) 2000135.
[78] K. Tang et al., Electrochim. Acta 312 (2019) 45–53.
[79] Q. Zhang et al., Sci. China Mater. 60 (2017) 629–636.
[80] Y. Wang et al., Chem. Eng. J. 360 (2019) 139–147.
[81] Y. Chen et al., J. Power Sources 397 (2018) 307–317.
[82] R. Muruganantham et al., Sci. Rep. 7 (2017) 14808.
[83] J.T. Incorvati et al., Chem. Mater. 28 (2016) 17–20.
[84] M. Inamoto et al., Materials (Basel) 6 (2013) 4514–4522.

Please cite this article in press as: F. Xiong et al., Materials Today, (2021), https://doi.org/10.1016/j.mattod.2020.12.002

[85] D. Aurbach et al., Adv. Mater. 19 (2007) 4260–4267.
[86] Z. Wang et al., Small 15 (2019) 1902797.
[87] Q. Yu et al., Chem. Eng. J. 396 (2020) 125218.
[88] Y. Zhang et al., Small 15 (2019) 1905452.
[89] L. Liu et al., Adv. Energy Mater. 5 (2015) 1500944.
[90] B. Zhang et al., J. Alloys Comp. 728 (2017) 976–983.
[91] J.-Y. Hwang et al., J. Mater. Chem. A 4 (2016) 17952–17959.
[92] D. Kim et al., Adv. Energy Mater. 1 (2011) 333–336.
[93] H. Yoshida et al., Chem. Commun. 50 (2014) 3677–3680.
[94] D. Yuan et al., Electrochim. Acta 116 (2014) 300–305.
[95] Y. Hou et al., Mater. Today: Energy 14 (2019) 100353.
[96] D. Buchholz et al., Electrochim. Acta 110 (2013) 208–213.
[97] M. Ben Yahia et al., Nat. Mater. 18 (2019) 496–502.
[98] H. Xu et al., J. Mater. Chem. A 7 (2019) 23662–23678.
[99] J. Jin, et al., Sci. China Chem. (2020).
[100] U. Maitra et al., Nat. Chem. 10 (2018) 288–295.
[101] X. Zhang et al., Adv. Mater. 31 (2019) 1807770.
[102] R.A. House et al., Chem. Mater. 31 (2019) 3293–3300.
[103] X. Cao et al., ACS Energy Lett. 4 (2019) 2409–2417.
[104] S. Komaba et al., Inorg. Chem. 51 (2012) 6211–6220.
[105] N. Yabuuchi et al., Nat. Mater. 11 (2012) 512–517.
[106] J.S. Thorne et al., J. Electrochem. Soc. 161 (2014) A2232–A2236.
[107] H.-R. Yao et al., J. Am. Chem. Soc. 139 (2017) 8440–8443.
[108] H. Kim et al., J. Am. Chem. Soc. 134 (2012) 10369–10372.
[109] T. Yuan et al., Nano Energy 56 (2019) 160–168.
[110] H. Kim et al., Energy Environ. Sci. 8 (2015) 3325–3335.
[111] M. Nose et al., J. Power Sources 234 (2013) 175–179.
[112] H. Zhang, et al., NPG Asia Mater. 9 (2017) e370-e370.
[113] C. Zhan et al., Energy Environ. Sci. 11 (2018) 243–257.
[114] H. Chen et al., Electrochim. Acta 308 (2019) 64–73.
[115] L.F. Wan et al., Chem. Mater. 28 (2016) 6900–6908.
[116] M. Mao et al., Chem. Mater. 31 (2019) 3183–3191.
[117] H. Tang et al., Nano Energy 58 (2019) 347–354.
[118] P. He et al., Adv. Energy Mater. 8 (2018) 1702463.
[119] F. Tang et al., Electrochim. Acta 328 (2019) 135137.
[120] Y.-H. Zhu et al., Chem 5 (2019) 168–179.
[121] K. Yuan et al., Energy Technol. 8 (2019) 1900796.
[122] M. Clites et al., ACS Energy Lett. 3 (2018) 562–567.
[123] M. Tian et al., Energy Storage Mater. 29 (2020) 9–16.
[124] Y. Hao et al., ChemNanoMat 6 (2020) 797–805.
[125] G. Liu et al., J. Mater. Chem. A 7 (2019) 20806–20812.
[126] Y. Xu et al., Chem 5 (2019) 1194–1209.
[127] F. Ming et al., ACS Energy Lett. 3 (2018) 2602–2609.
[128] X. Xu et al., ACS Energy Lett. 4 (2019) 1328–1335.
[129] C. Xia et al., Angew. Chem. Int. Ed. 57 (2018) 3943–3948.
[130] M.S. Chae et al., ACS Appl. Energy Mater. 3 (2020) 5107–5112.
[131] T. Sun et al., Small 16 (2020) 2000597.
[132] Q. Wei et al., ACS Appl. Mater. Interfaces 7 (2015) 18211–18217.
[133] J. Li et al., Adv. Energy Mater. 10 (2020) 2000473.
[134] C. Liu et al., Energy Environ. Sci. 12 (2019) 2273–2285.
[135] X. Deng et al., J. Mater. Chem. A 7 (2019) 10644–10650.
[136] D. Kundu et al., Nat. Energy 1 (2016) 16119.
[137] C. Liu et al., Mater. Today: Energy 11 (2019) 218–227.
[138] Y. Zhao et al., Nano Lett. 15 (2015) 2180–2185.
[139] S. Li et al., J. Alloys Comp. 801 (2019) 82–89.
[140] M. Clites, E. Pomerantseva, Energy Storage Mater. 11 (2018) 30–37.
[141] Y. Yang et al., Nano Energy 61 (2019) 617–625.
[142] B. Mortemard de Boisse, et al., Adv. Energy Mater. 8 (2018) 1800409.
[143] Y. Li et al., Adv. Energy Mater. 9 (2019) 1803087.
[144] Y. Shang et al., Chem 6 (2020) 1804–1818.
[145] C. Zhu et al., Energy Storage Mater. 24 (2020) 394–401.
[146] N. Zhang et al., J. Am. Chem. Soc. 138 (2016) 12894–12901.
[147] L. Luo et al., Nano Energy 72 (2020) 104716.
[148] T. Koketsu et al., Nat. Mater. 16 (2017) 1142–1148.
[149] Y. Wang et al., ACS Nano 12 (2018) 12492–12502.
[150] Z. Li et al., ACS Nano 14 (2020) 5581–5589.
[151] H. Luo et al., Energy Storage Mater. 33 (2020) 390–398.
[152] M. Liao et al., Angew. Chem. Int. Ed. 59 (2020) 2273–2278.
[153] Y. Lin et al., ChemSusChem 13 (2020) 3696–3706.
[154] W. Yang et al., Small Meth. 4 (2019).
[155] T. Xiong et al., Adv. Energy Mater. 9 (2019) 1803815.
[156] G. Fang et al., Adv. Funct. Mater. 29 (2019) 1808375.
[157] J. Tu et al., Chem. Commun. 54 (2018) 1343–1346.
[158] Y. Li et al., J. Mater. Chem. A 4 (2016) 5402–5405.
[159] H. Xia et al., Nat. Commun. 9 (2018) 5100.
[160] Y. Zhang et al., Small Meth. 4 (2020) 1900828.
[161] S. Song et al., ACS Sustain. Chem. Eng. 5 (2017) 4785–4792.
[162] S. Song et al., Sci. Rep. 7 (2017) 373.
[163] Y. Xu et al., Angew. Chem. Int. Ed. 54 (2015) 8768–8771.
[164] H. Zhang et al., Energy Storage Mater. 21 (2019) 154–161.
[165] Z.W.J. Ang et al., ChemNanoMat 6 (2020) 1357–1364.
[166] M. Han, et al., iScience 23 (2020) 100797.
[167] C. Ma et al., J. Am. Chem. Soc. 139 (2017) 4835–4845.
[168] S. Guo et al., Sci. Bull. 63 (2018) 376–384.
[169] K. Sato et al., Chem. Mater. 29 (2017) 5043–5047.
[170] J. Lee et al., Science 343 (2014) 519–522.
[171] Y. Wang et al., Nat. Commun. 6 (2015).
[172] S.M. Kang et al., ACS Appl. Mater. Interfaces 10 (2018) 3562–3570.
[173] L. Mai et al., Nano Lett. 10 (2010) 4273–4278.
[174] J. Huang et al., Science 330 (2010) 1515–1520.
[175] E. Uchaker et al., J. Mater. Chem. A 2 (2014) 18208–18214.
[176] S. Liu et al., PCCP 18 (2016) 25645–25654.
[177] X. Wang et al., Adv. Energy Mater. 10 (2020) 2000081.
[178] Y. Cheng et al., Adv. Funct. Mater. 26 (2016) 3446–3453.
[179] M. Chiku et al., ACS Appl. Mater. Interfaces 7 (2015) 24385–24389.
[180] Y. Wu et al., ACS Appl. Energy Mater. 3 (2020) 1627–1633.
[181] Y. Cai et al., Chem. Eng. J. 396 (2020) 125221.
[182] S. Bi et al., Mater. Today: Energy (2020) 100548.
[183] Q.D. Truong et al., Nano Lett. 16 (2016) 5829–5835.
[184] V. Mathew, et al., NPG Asia Mater. 6 (2014) e138-e138.
[185] S.Y. Lim et al., ACS Energy Lett. 2 (2017) 998–1004.
[186] Y. Fang et al., Nano Lett. 14 (2014) 3539–3543.
[187] T. Liu et al., J. Mater. Chem. A 4 (2016) 4479–4484.
[188] G. Yang et al., Nanoscale 8 (2016) 8495–8499.
[189] Y. Liu et al., Nano Lett. 12 (2012) 5664–5668.
[190] F. Xiong et al., Nano Energy 57 (2019) 608–615.
[191] J. Kim et al., Energy Environ. Sci. 8 (2015) 540–545.
[192] R. Kapaev et al., J. Solid State Electrochem. 21 (2017) 2373–2380.
[193] S. Nakata et al., J. Non-Cryst. Solids 450 (2016) 109–115.
[194] Q. Wei et al., J. Mater. Chem. A 3 (2015) 8070–8075.
[195] Y. Zhang et al., Nano Energy 57 (2019) 592–599.
[196] Y. Zhang et al., Nano Energy 49 (2018) 596–602.
[197] C. Tang et al., Chem. Eng. J. 382 (2020) 123049.
[198] Y. Yuan et al., Joule 3 (2019) 471–484.

Please cite this article in press as: F. Xiong et al., Materials Today, (2021), https://doi.org/10.1016/j.mattod.2020.12.002